HORIZON EUROPE PROGRAMME

TOPIC HORIZON-CL4-2022-RESILIENCE-01-24

GA No. 101091572

Graphene, MXene and ionic liquid-based sustainable supercapacitor

GREEN CAP

GREENCAP - Deliverable report

D1.3 – Multiscale characterization of EMs and electrolytes

Funded by the European Union

Deliverable No.	GREENCAP D1.3	
Related WP	WP 1	
Deliverable Title	Multiscale characterization of EMs and electrolytes	
Deliverable Date	2024-12-31	
Deliverable Type	REPORT	
Dissemination level	Public (PU)	
Author(s)	Prof Andrea Ferrari (UCAM) Dr Boyang Mao (UCAM)	
Checked by	Prof. Valeria Nicolosi (TCD)	2024-12-09
Reviewed by (if applicable)	Paolo Samorì (UNISTRA) Ali Shaygan Nia (TUD)	2024-12-10 2024-12-16
Approved by	Francesco Bonaccorso (BED) - Project coordinator	2024-12-31
Status	Final	2024-12-31

Document History

Version	Date	Editing done by	Remarks
V1.0	28/11/2024	Andrea Ferrari, Boyang Mao (UCAM)	First draft
V2.0	09/12/2024	Valeria Nicolosi	TCD amended and reviewed
V3.0	10/12/2024	Paolo Samorì	UNISTRA added their part and reviewed
V4.0	16/12/2024	Ali Shaygan Nia	TUD added their part and reviewed
V5.0	31/12/2024	Francesco Bonaccorso	final

Project summary
GREENCAP aims to revolutionize the field of energy storage while meeting the EU's climate-neutrality goals and the Action Plan on Critical Raw Materials (CRMs). This multi-disciplinary consortium, consisting of partners from seven European countries and Ukraine, seeks to develop sustainable electrode materials for supercapacitors (SCs) that exhibit battery-like energy density, high power densities, and long cycle life. Utilizing graphene and MXenes as electrode materials and ionic liquids (ILs) for high-voltage electrolytes, GREENCAP will boost the material's specific surface area, ion accessibility, and charge storage while ensuring stability and safety across a wide temperature range. The project will validate this SC technology at an industrial scale (TRL 6) and develop a management system to optimize SC integration into high-end applications and the circular economy.

Publishable summary

D1.3 reports multiscale physicochemical and electrochemical characterization of electrode materials (EMs) and electrolytes, a key step toward developing sustainable, high-performance supercapacitors (SCs). The multiscale characterization tasks were distributed across the consortium, leveraging the diverse expertise of partner institutions. To ensure reliable and reproducible results, standardized characterization methodologies were established and applied uniformly across all products. We investigated the compositional, structural, morphological, and (electro)chemical properties of EMs, using Thermogravimetric analysis (TGA), Auger electron (AES), photoemission spectroscopy (PES), Raman spectroscopy and X-ray photoelectron spectroscopy (XPS), X-Ray diffraction analysis (XRD), atomic force microscopy (AFM), scanning electron microscopy (SEM) and high-resolution transmission electron microscopy (HRTEM), and gas physisorption analysis (BET). Complementary studies included electrolyte density and conductivity measurements across a wide temperature range (-20 °C to +80 °C) and flash point assessments. Electrochemical evaluations were performed using cyclic voltammetry (CV), galvanostatic charge-discharge (GCD), and electrochemical impedance spectroscopy (EIS). These findings lay the groundwork for understanding the electrical double-layer mechanisms at layered two-dimensional material and ionic liquid interfaces, ultimately guiding the rational design of next-generation SCs. Task 1.3 objectives have been successfully achieved.

Contents

List of Figures

List of Tables

Abbreviations & Definitions

Abbreviation	Explanation
2d	2 dimensional
CRM	Critical Raw Material
FSI	Bis(fluorosulfonyl)imide
IL	Ionic Liquids
L2DM	Layered 2D material
EM	Electrode Material
SC	Supercapacitor
TFO	Triflate
TFSI	Bis(trifluoromethanesulfonyl)imide
N1113	N-Trimethyl-N-propylammonium
TEA	Tetraethylammonium
CG	Curved graphene
WJM	Wet-jet milling
AC	Activated carbon
HPH	High-Pressure Homogenisation
FLG	Few layer Graphene
GCD	Galvanostatic charge/discharge
PXRD	Powder X-ray Diffraction
XPS	X-ray photoelectron spectroscopy
XRD	X-Ray diffraction analysis
AFM	Atomic force microscopy
HRTEM	High-resolution transmission electron microscopy
CV	Cyclic voltammetry
GCD	Galvanostatic charge-discharge
EIS	Electrochemical impedance spectroscopy
ACN	Acetonitrile
GVL	Gamma-valerolactone
FWHM	Full width at half maximum
TGA	Thermogravimetric analysis
AES	Auger electron
PES	Photoelectron

1 Introduction

D1.3 covers multiscale physicochemical and electrochemical characterization of EMs and electrolytes. The reported activities focused on analyzing the compositional, structural, morphological, and (electro)chemical properties of the materials. These characterizations provide critical insights into optimizing SC performance and contribute to achieving the project's overarching goals of developing sustainable, high-performance energy storage solutions. The multiscale characterization tasks were distributed across the consortium, leveraging the expertise of partner institutions. Key activities included:

- **Compositional Characterization**: Techniques such as thermogravimetric analysis (TGA), Auger electron (AES), photoemission spectroscopy (PES), X-ray photoelectron spectroscopy (XPS), and X-Ray diffraction analysis (XRD), Raman Spectroscopy were used.
- **Structural/Morphological and Physical Characterization**: These assessments were conducted using advanced microscopy techniques such as atomic force microscopy (AFM), scanning electron microscopy (SEM) coupled with atomic resolution EDX, high-resolution transmission electron microscopy (HRTEM), and gas physisorption analysis (BET method). Electrolyte density and ionic conductivity measurements complemented over a temperature range between -20 °C to +80 °C, as well as flash point determinations, complemented these analyses.
- **Electrical and Electrochemical Characterization**: Cyclic voltammetry (CV), galvanostatic charge-discharge (GCD), and electrochemical impedance spectroscopy (EIS).

These efforts underpin the foundational knowledge required for modeling the electrical double-layer structure at the interfaces of layered two-dimensional materials and ionic liquid-based electrolytes, thereby guiding the rational design of advanced SCs. The objectives in Task 1.3 have been achieved.

2 Methods and core part of the report

UCAM evaluated the quality of Few Layer Graphene (FLG) EMs by measuring Raman spectra at each stage of material processing. Raman analysis was performed on both High-Pressure Homogeniser (HPH) processed Synthetic Graphite and Expanded Synthetic Graphite, the latter produced via acid intercalation and microwave treatment. There is a small increase in the ratio of intensity of D band over the intensity of G band, I(D)/I(G) from ~ 0.08 to ~ 0.11, which indicates that the expansion process introduces additional defects. Considering then the I(D)/I(G) (**Figure 1**) as a function of cycle number we observe a small increase and subsequent saturation for both materials. For synthetic graphite, I(D)/I(G) saturates after 50 HPH cycles, whereas for expanded synthetic graphite I(D)/I(G) saturates at less than 20 HPH cycles. The increase, and saturation, of I(D)/I(G) occurs due to decreasing lateral flake size with increasing number of HPH cycles. The saturation of the I(D)/I(G) for the expanded graphite at lower HPH cycle number is consistent with the increase in layer separation for the expanded material. FWHM (G) (**Figure 2**) shows no significant variation with HPH cycle number and indicates that level of disorder in the material is not increasing with cycle number.

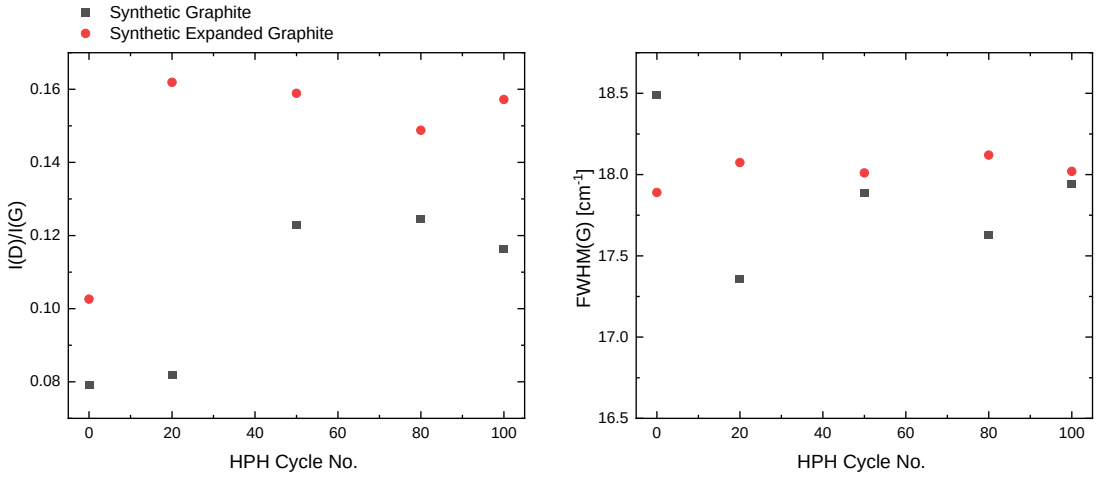

Figure 1 *I(D)/I(G) (Left panel) and FWHM (G) (right panel) for synthetic (grey) and expanded synthetic graphite (red) as a function of HPH cycle number.*

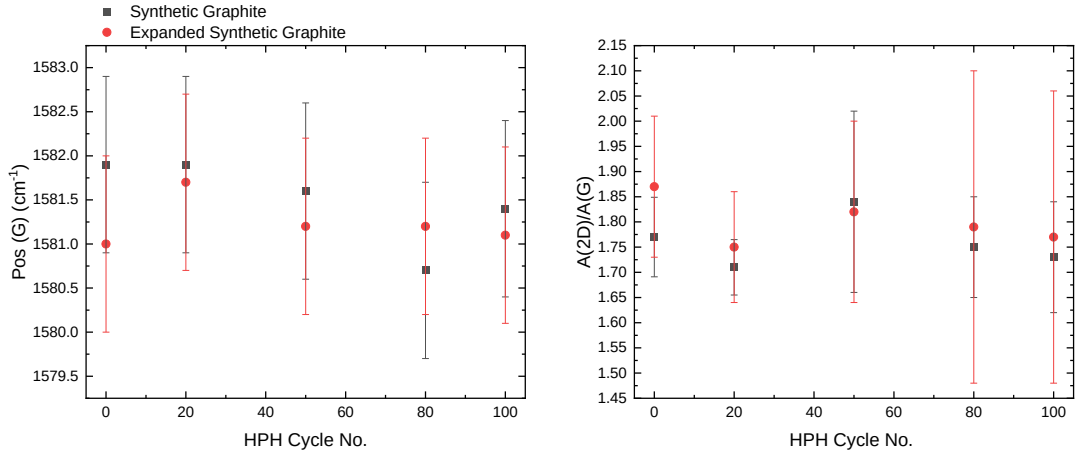

Figure 2 *Position of the G peak (left panel) and A(2D)/A(G) (right panel) are shown for synthetic (grey) and expanded synthetic graphite (red) as a function of HPH cycle number.*

This confirms that the increase in (D)/I(G) is due to decreasing lateral flake size and indicates that HPH does not introduce additional disorder in the exfoliated flakes. Furthermore, the position of G peak,

Pos(G) (Figure 3) shows no significant variation due to starting material (synthetic or expanded graphite) or on the number of HPH cycles. This suggests that both the homogenisation and expansion process do not introduce significant strain or doping in the samples. Finally, for the ratio of area of 2D peak over the area of G peak, A(2D)/A(G) (Figure 2) neither number of HPH cycles nor starting material shows a significant change, which is in line with the consistently graphitic nature of the flakes as seen from the initial spectra.

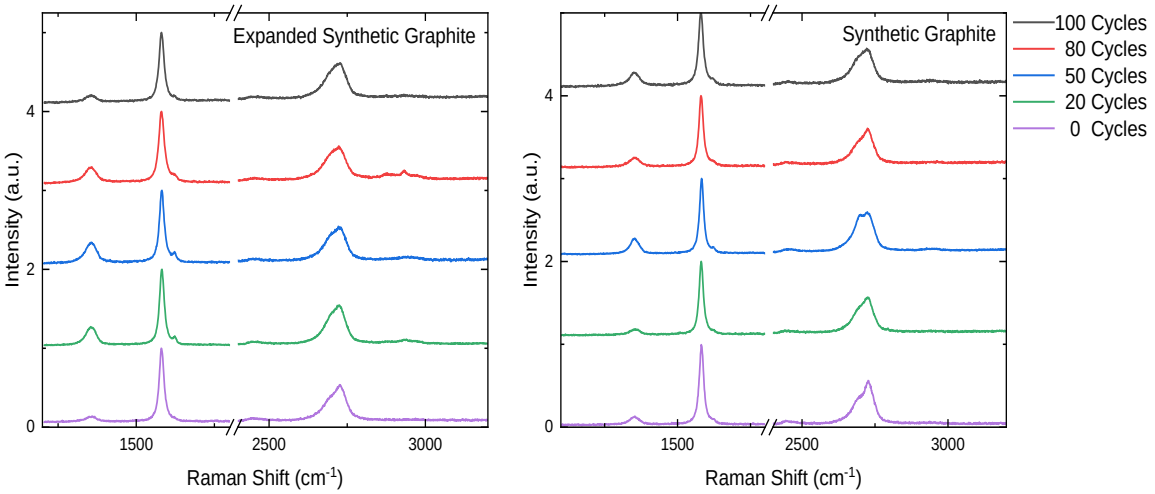

Figure 3 *Representative Raman spectra of HPH exfoliated graphite produced using (left) synthetic graphite and (right) expanded synthetic graphite produce by acid intercalation and microwave treatment and show spectra after 0, 20, 50,80 and 100 HPH cycles.*

UCAM has also performed Raman characterisation on curved graphene, produced by **Skeleton**, and MXene materials from **TCD.** Skeleton's curved graphene is produced from carbide derived carbon (CDC) and is subject to several processing steps such as chlorination, hydrogen treatment and ball milling. As shown in **Figure 4** the Raman spectra for Skeleton's material consist of two broad peaks at ~ 1360 and ~ 1600 cm^{-1} consistent with the D and G Raman peaks observed for nanocrystalline or amorphous carbons.

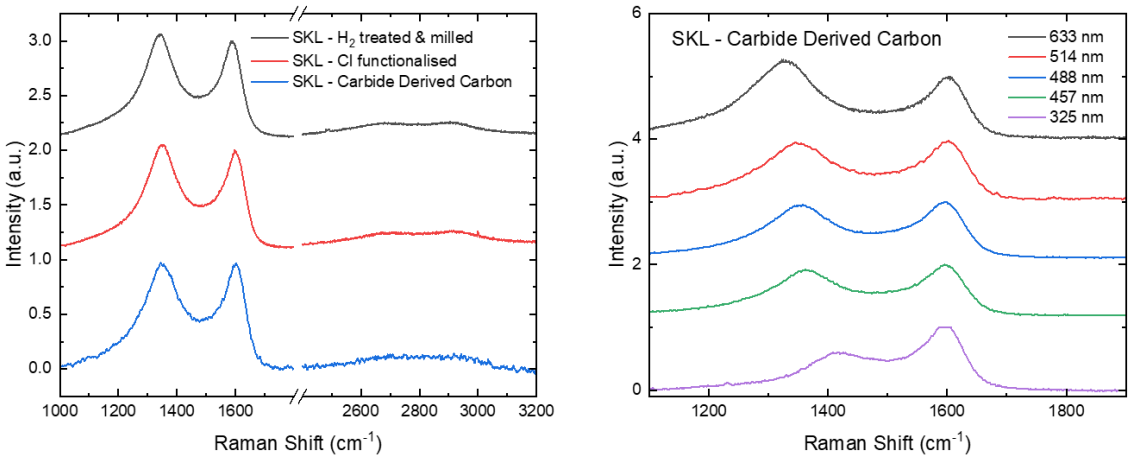

Figure 4 *(Left) Representative Raman spectra for Skeleton's carbon derived carbon at different stages in the materials processing. (Right) Representative multiwavelength Raman spectra for Skeleton's starting material, carbide-derived carbon.*

In **Figure 5**, by comparing I(D)/I(G) there is no significant variation in the ratio for the different material processing steps of the CDC. The broad nature of the D and G peaks is evident in the FWHM which are ~ 110 to 150 cm^{-1} and 70 to 78 cm^{-1} respectively. For FWHM(G) we observe no significant change, however, we do observe a significant decrease in the standard deviation for the ball-milled and H_2 treated material. This suggests that the ball milling and hydrogen treatment have led to a more homogeneous material.

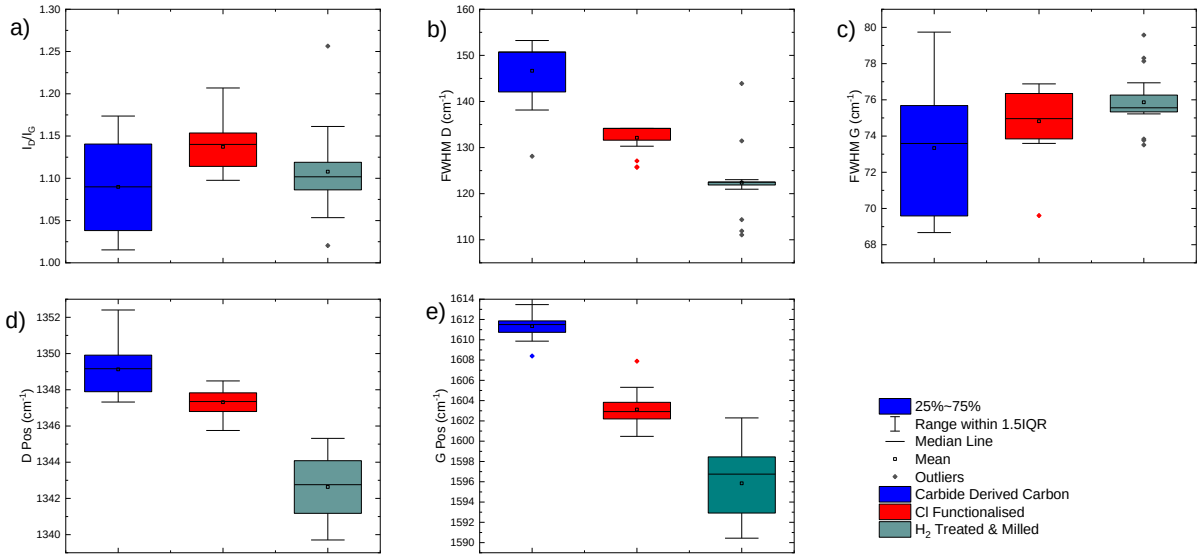

***Figure 5**. Raman analysis for Skeleton CDC (blue), Cl functionalised (red), H_2 treated, ball milled (green). (a) I(D)/I(G), (b) FWHM (D), (c) FWHM (G), (d) Pos (D), (e) Pos (G).*

Multiwavelength Raman spectroscopy was then performed. For Skeleton's CDC and **UCAM**'s synthetic graphite the G peak dispersion is shown in Figure 6. The higher dispersion of Pos(G) for CDC indicates it is likely nanocrystalline graphite. I(D)/I(G) can be used to derive a mean length of the sp^2 carbon domains~ 3.8 ± 0.1 nm.

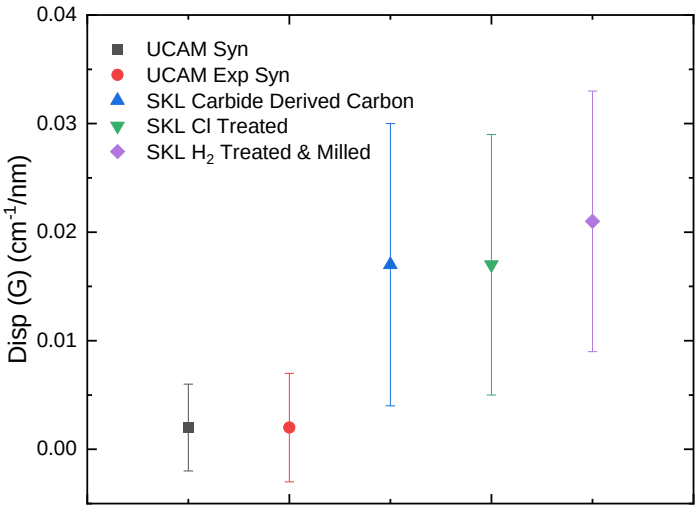

***Figure 6** Dispersion of the G peak determined from multiwavelength Raman for UCAM synthetic and expanded synthetic graphite, and Skeleton's CDC at different stages in processing.*

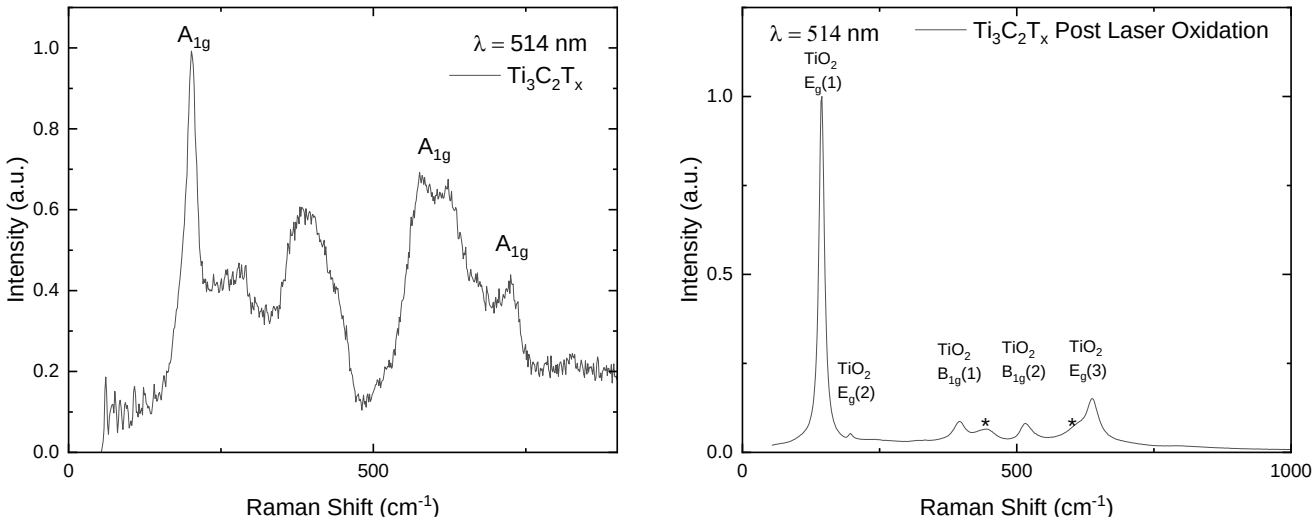

***Figure 7** (Left) Representative Raman spectra for $Ti_3C_2T_X$. (Right) Raman spectra of $Ti_3C_2T_X$ after exposure to laser powers >1mW to oxidise the material forming TiO_2 and amorphous carbon.*

The sensitivity of MXene materials to processing conditions i.e., etchant, temperature, and exposure to oxygen can be mitigated by application of Raman spectra to assess the chemical stability of the materials. UCAM acquired Raman spectra on Ti_3C_2X powders and slurries (**Figure 7**). Application of laser power in excess of 1mW leads to the oxidation of the MXene, forming both rutile and anatase phases of TiO_2 alongside the formation of an amorphous carbon which leads to the appearance of a D band at ~ 1360 cm^{-1}. Understanding the thermal stability of MXene may be useful for the development of electrode materials for high-temperature applications.

BED reported a systematic study of the effect of a prototypical treatment, i.e. H_2-assisted thermal treatments, on the chemical, structural and thermal properties of activated carbon and corresponding electrodes based on FLG as the conductive additives. By combining multiple characterization techniques, including XPS, XRD, Raman spectroscopy and TGA (**Figure 8-Figure 10**), we shed light on the improvement of the performance (*e.g.*, >+35% energy density for the investigated power densities in the 0.5-45 kW kg^{-1} range) of the double-layer capacitors based on treated electrodes compared to the case based on the pristine electrodes. Despite single characterization techniques indicating surface graphitization of active materials accompanied by the desorption of surface contaminants, our holistic approach identifies the change in the active material and binder content and the cleaning of the activated carbon surface as a concomitant cause of the increase of gravimetric capacitance (C_g), accounting for all the electrode materials, measured for treated electrodes compared to pristine ones. The elimination of surface impurities, including adsorbed species, improves the surface capacitance of the activated carbon (C_{surfAC}) by +37.1% and +36.3% at the specific currents of 1 and 10 A g^{-1}, respectively. Despite the trade-off between chemical ("surface graphitization") and structural (densification) effects upon the thermal treatment, the latter significantly improves the C_g of the activated carbon only (C_{gAC}), e.g., +28% at 1 A g^{-1}.

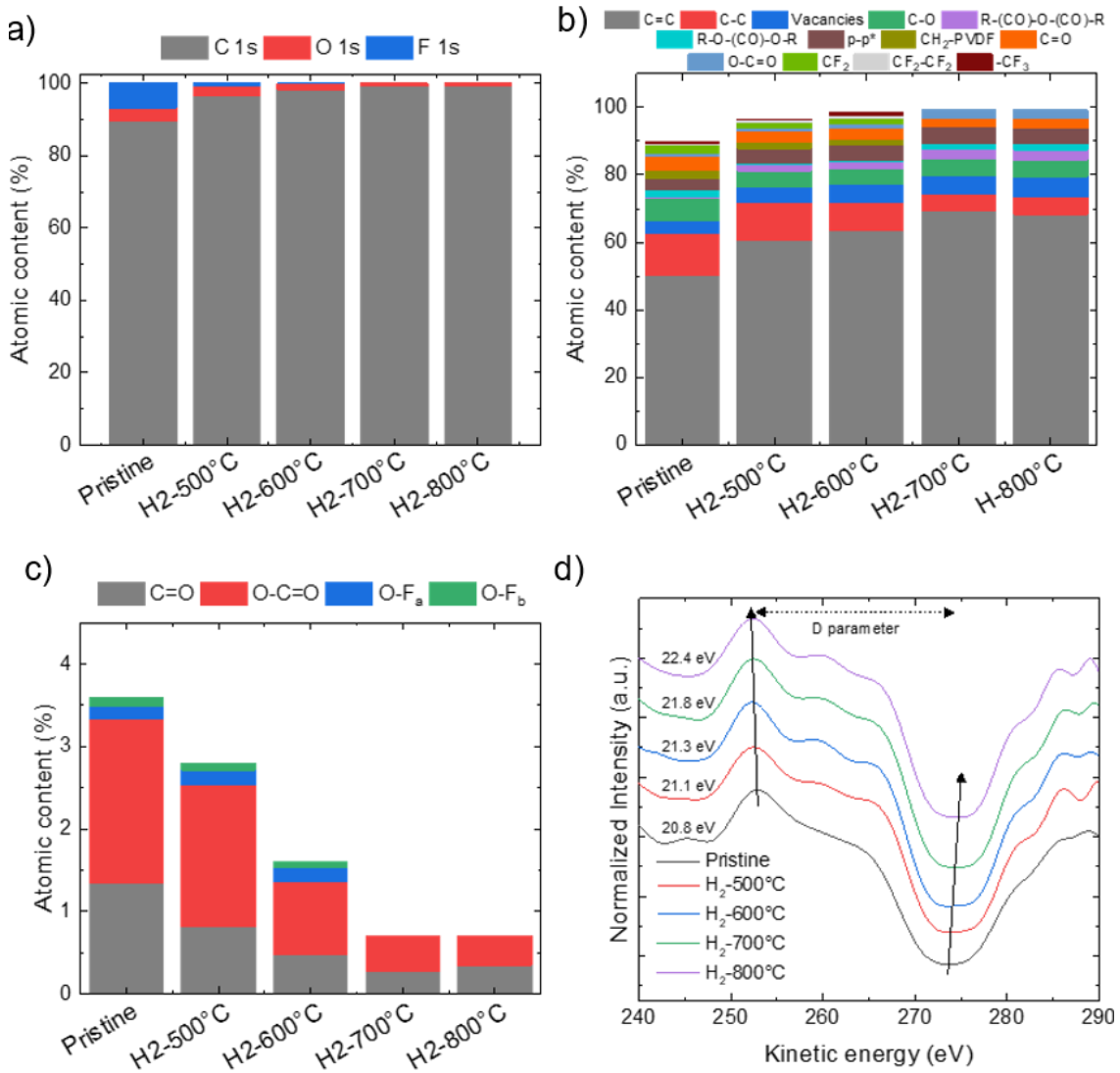

***Figure 8**. a) Elemental composition of EMs before and after H_2-assisted thermal treatment at various temperatures (from 500 °C to 800 °C). b) C and c) O functionalities at% (normalized on the overall C and at%, respectively) of the investigated electrode materials. The data have been estimated from the analysis of the XPS spectra (wide scan, C 1s, and O 1s spectra). d) The first derivative of the XAES C KLL spectra (parameter D) of the investigated electrode materials.*

Aiming to improve the electrochemical stability of SCs based on CG:FLG electrodes and N_{1113}FSI-based electrolytes, BED investigated the mass balance between the positive and the negative electrodes. The study focused on electrodes composed of CG or AC as the active material, FLG as the conductive agent, and carboxymethyl cellulose and styrene-butadiene rubber, CMC/SBR (1/2.75) as the aqueous binder, with a composition ratio of 94:2:4 by weight (CG:FLG:CMC/SBR or AC:FLG:CMC/SBR). The electrolytes employed were 1 M N_{1113}FSI in acetonitrile (ACN) and 1 M N_{1113}FSI in γ-Valerolactone (GVL). The electrochemical stability voltage window in a three-electrode Swagelok cell was evaluated using cyclic voltammetry (CV) at a scan rate of 50 mV s^{-1}, with high-mass-loading AC counter electrodes (Figure 11). A silver wire, directly immersed in the electrolyte, served as a pseudo-reference electrode.

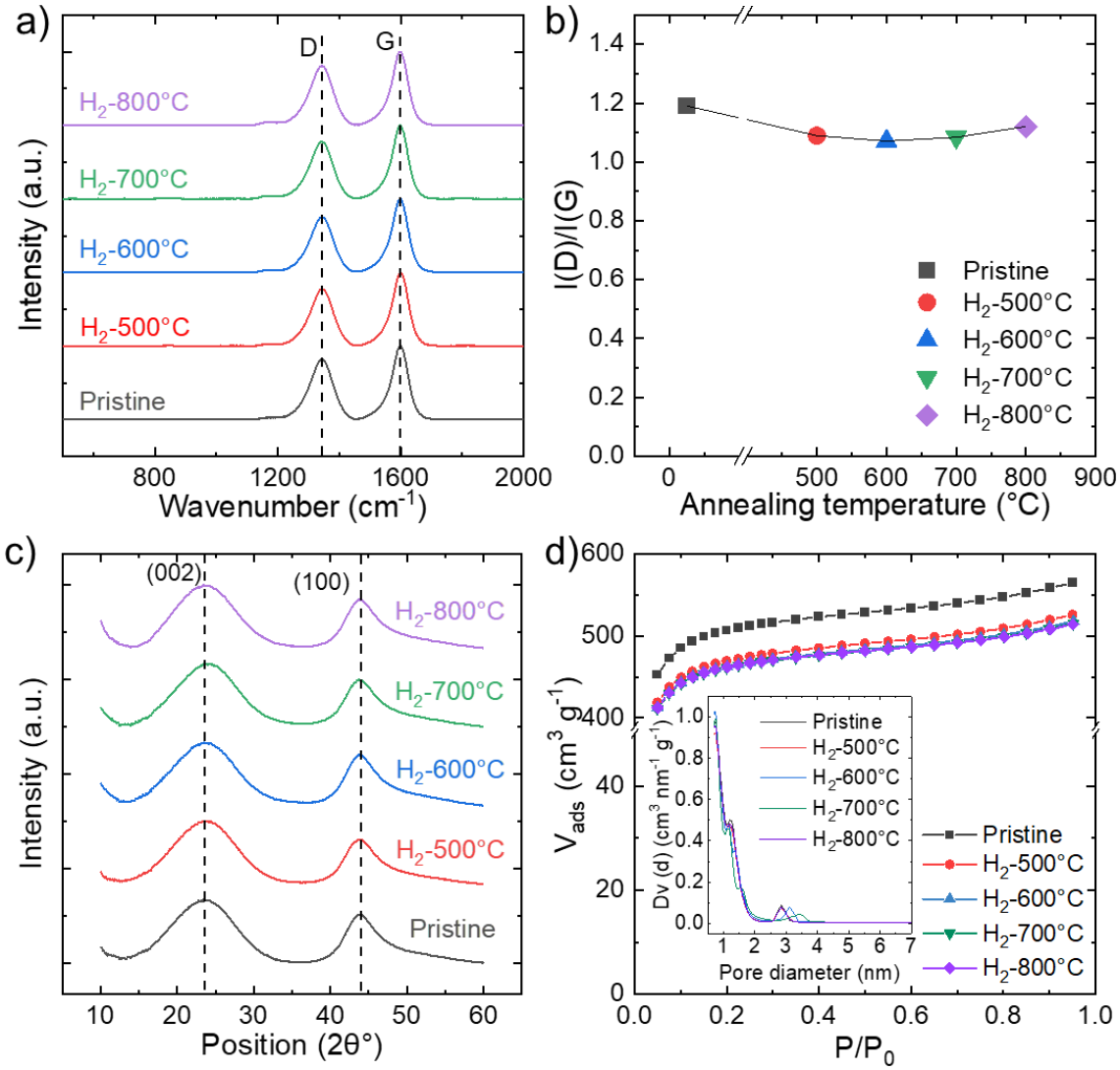

***Figure 9**. Structural characterization of the activated carbon before (pristine) and after the H_2-assisted thermal treatments at various temperatures (H_2-500°C, H_2-600°C, H_2-700°C and H_2-800°C). a) Raman spectra and b) I(D)/I(G) vs. annealing temperature. c) XRD patterns. d) N_2 adsorption/desorption isotherms before (pristine) and after H_2-assisted thermal treatments at various temperatures (H_2-500°C, H_2-600°C, H_2-700°C and H_2-800°C). The inset panel shows the PSD, calculated by applying the QSDFT to the Ar adsorption data at 87 K, for the investigated electrode materials.*

As shown in **Figure 11**, all samples exhibit semi-EDLC to EDLC behaviour. All the samples demonstrated similar behaviour in the N_{1113}FSI/ACN electrolyte (Figures 11a and 11b). Notably, CG achieved the widest electrochemical stability window, nearing 3.5 V. Switching the solvent from ACN to GVL significantly impacted the electrochemical behaviour of the samples. In the presence of GVL, the CV curves deviate from the ideal EDLC profile (Figures 11c and 11d), especially for CG-based electrodes, which exhibited a non-rectangular CV curve shape, indicating reduced compatibility with the N_{1113}FSI/GVL electrolyte. In detail, the area enclosed in the CV curve is notably reduced for negative potentials, in which the cations diffuse in the electrode. This difference suggests a mismatch between the pore structure of CG and the solvation sphere of N_{1113}^+ ions in GVL. Specifically, compared to ACN, GVL generates a larger solvation radius due to its larger molecule size. This hinders the N_{1113}^+ ions diffusion within the micropores of CG, ultimately diminishing the CG performance when used as

negative electrode with the N1113FSI/GVL electrolyte. In order to confirm those insights, the diffusion of N_{1113}^+ is currently under investigation by means of electrochemical impedance spectroscopy.

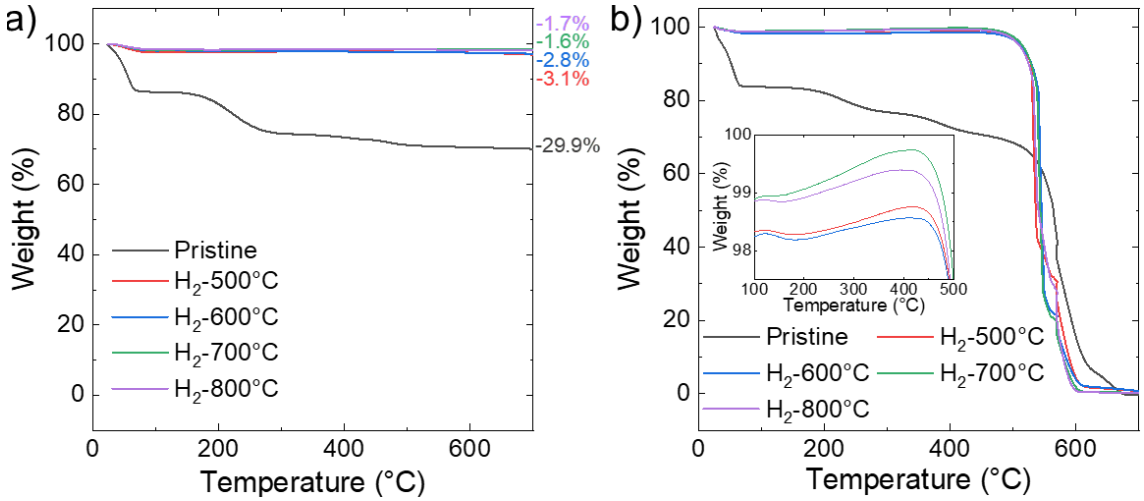

***Figure 10**. TGA curves measured in a) N_2 and b) O_2 for activated carbons before (pristine) and after H_2-assisted thermal treatments at various temperatures (H_2-500°C, H_2-600°C, H_2-700°C and H_2-800°C).*

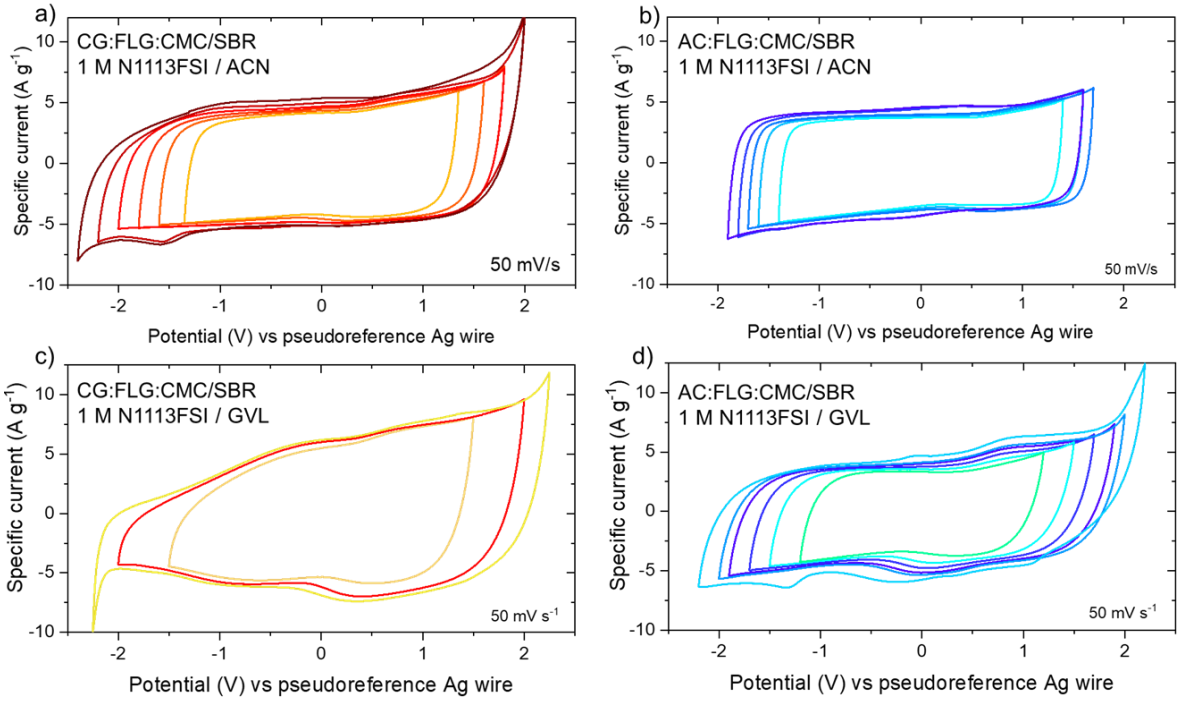

***Figure 11**: CV in three-electrode system of various electrodes materials using N1113FSI-based electrolytes and high mass loading AC counter electrodes. a) CV cycles of CG:FLG-based electrode with N1113FSI/ACN electrolyte; b) CV cycles of AC:FLG-based electrode with N1113FSI/ACN electrolyte; c) CV cycles of CG:FLG-based electrode with N1113FSI/GVL electrolyte; d) CV cycles of AC:FLG-based electrode with N1113FSI/GVL electrolyte.*

Initially, **BED** studied the AC:FLG-based SCs with N_{1113}FSI/ACN electrolyte, optimizing the mass ratio between the positive and the negative electrodes. The mass balance was refined performing galvanostatic charge-discharge cycles on a 3-electrode cell, monitoring both positive and negative

potentials. The charge balance between positive and negative electrodes resulted in a coulombic efficiency as high as 96.6 % and a gravimetric capacity as high as 53 mAh g^{-1} at 3.6 V (**Figure 12a**).

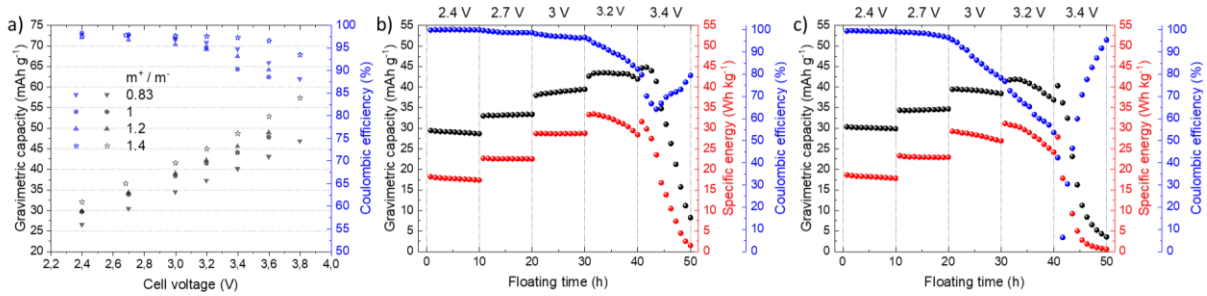

***Figure 12**: Electrochemical characterization of AC:FLG:CMC-SBR (94:2:4) -based SCs . a) gravimetric capacity and coulombic efficiency calculated from three-electrodes galvanostatic charge-discharge cycles as a function of the cell voltages; b) floating cycles of the SC with mass ratio m+/m- = 1.2; c) floating cycles of the SC with mass ratio m+/m- = 1.*

The floating tests performed on AC:FLG-based SC with a mass ratio of 1.2 (**Figure 12 b**) exhibited an increase of the electrochemical stability with respect to the SC with a mass ratio of 1 (**Figure 12 c**). The former reached a gravimetric capacity of 40 mAh g^{-1} and 96% of coulombic efficiency at 3.0 V. The optimization of the mass ratio between the CG:FLG-based electrodes and the characterization with floating tests are currently undergoing.

Since the CG:FLG-based electrodes are shown to underperform with the N_{1113}^{+} ions in GVL, **BED** follow a different strategy in order to exploit both the superior electrochemical stability of CG and the use of GVL as an eco-sustainable and safe solvent. An asymmetric SC based on CG:FLG and AC:FLG as positive and negative electrodes, respectively, is under investigation combining the higher electrochemical stability of the former with the higher compatibility of the latter with the solvated cations. As a comparison, symmetric SCs are built and characterized as well. **Figure 13** shows the CV characterization of the devices with the ratio between the electrode masses equal to 1. The asymmetric device (**Figure 13a**) exhibited an increased electrochemical stability at high voltages compared to the symmetric SCs (**Figure 13b and c**). A deeper electrochemical characterization of the asymmetric SCs is currently undergoing with floating tests and GCD cycles as well as optimization of the mass ratio.

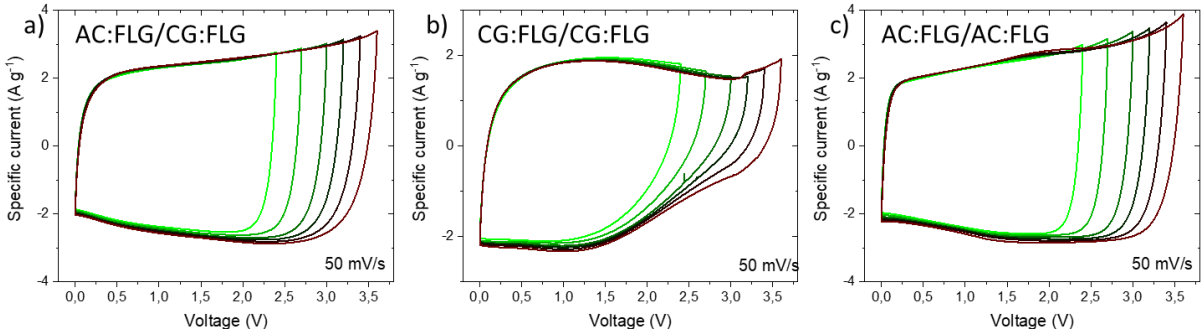

***Figure 13** Two-electrodes CV curves of SCs based on CG:FLG, AC:FLG electrodes and N1113FSI / GVL electrolyte with positive-negative electrode mass ratio of 1. a) symmetric device based on CG:FLG elctrodes; b) symmetric SC based on AC:FLG electrodes; c) asymmetric device with AC:FLG-based negative electrode and CG:FLG-based positive electrode.*

CV is a powerful electrochemical technique widely employed for investigating the redox behaviour and electrochemical properties of materials. **TUD** used CV for testing various materials. In the below list, the material and electrolytes are indicated, including both graphene and MXene materials (**Figure 14**).

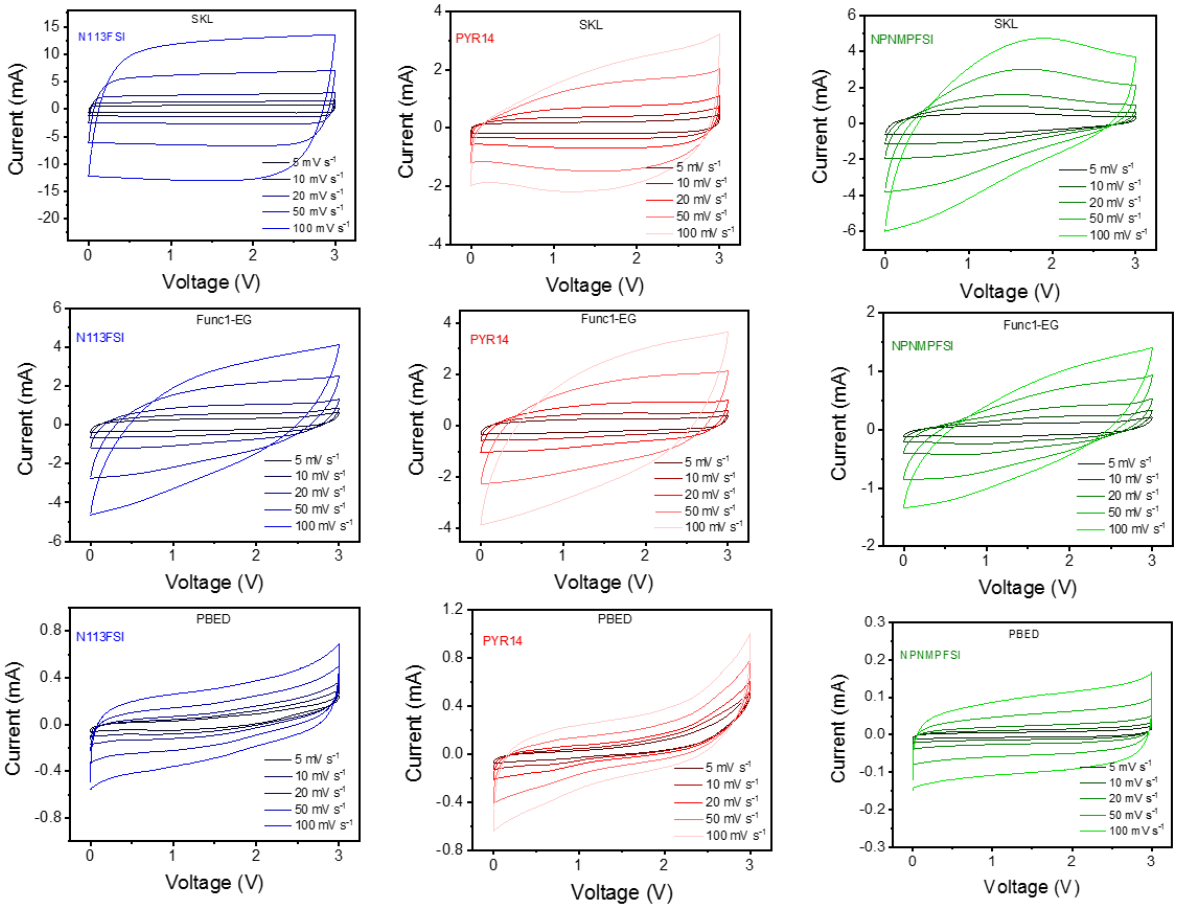

***Figure14**. CV of symmetric two-electrode cells (Al current collector, mass loading: 1-2 mg cm^{-2}).*

BED expressed the performance of all the electrode materials by means of capacity (based on one electrode weight) as a function of the scan rate (**Figure 15**). As a result, the **SKL** electrode with $N_{1113}FSI$ electrolyte has the highest capacity (26.5 F g^{-1}), while other materials are proposed as advanced conductive additives.

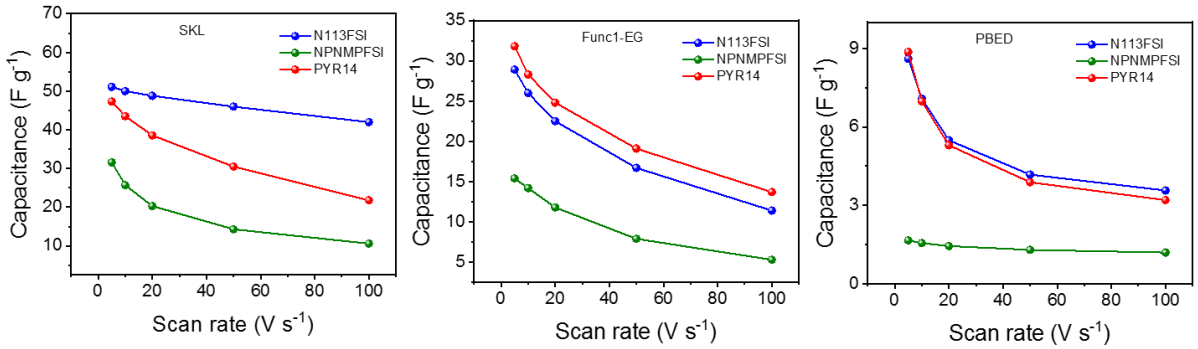

***Figure 15**. Comparison of capacitance for various electrode materials in combination with different IL-based electrolytes.*

BED also measured the CV of MXene electrode (Ti_3C_2 (Delaminated)) in three-electrode cells, using an Ag wire as the reference electrode (**Figure 16**). **BED** found that the $Pyr_{1H}TFO$ in ACN has the highest performance with MXene electrode (112 F g^{-1}).

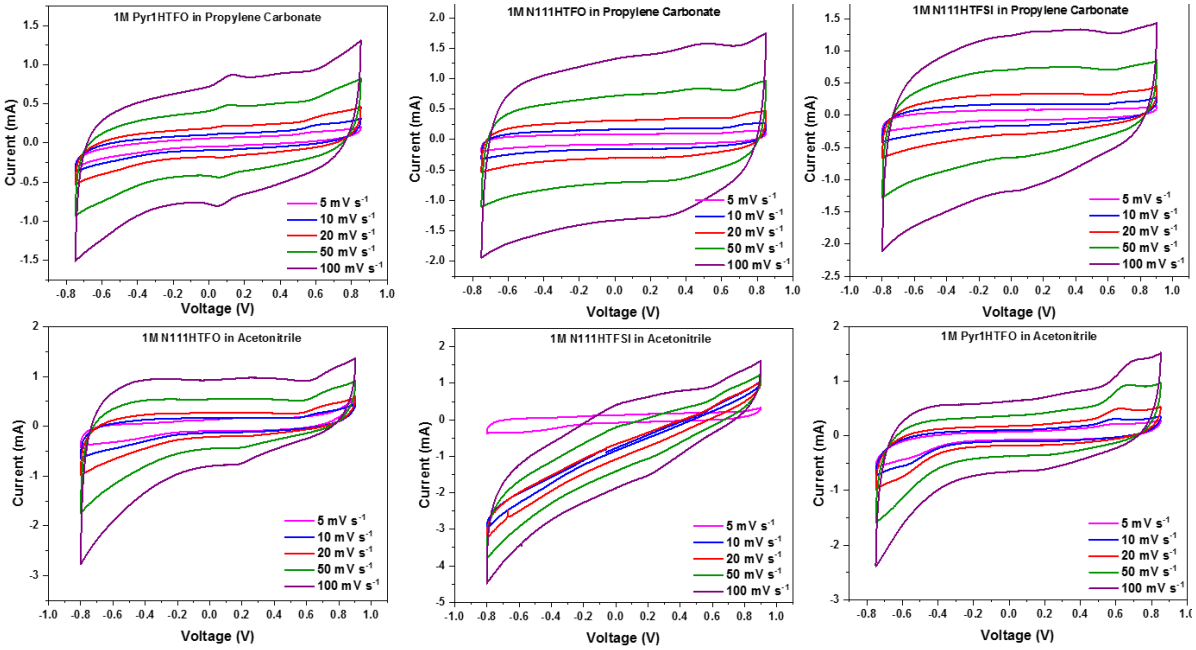

***Figure 16**. CV of MXene electrode in different IL electrolytes (1 M Pyr_{1H}TFO-PC, 1 M N_{111H}TFO-PC, 1 M N_{111H}TFSI-PC, 1 M N_{111H}TFO-CAN, 1 M N_{111H}TFSI-CAN, 1 M Pyr_{1H}TFO-ACN).*

SEM, EDX, TEM, EELS, and XRD measurements were performed at **TCD** to evaluate the crystalline phase, microstructure, and quality of the produced MXenes (see T1.1 activities).

UNISTRA performed XPS analyses on CG samples, provided by SKL, at different stages of the production process: SiC-Desorbed-Milled-H_2 treated samples. The primary objective was to identify the existence of chlorine covalently bonded to the carbon atoms within the samples. XPS analysis revealed that the sample at the second step of the production of curved graphene, known as milled, contained C-Cl covalent bonds that will be used for further functionalization. Additionally, all these samples were characterized by Raman spectroscopy, PXRD and by S_{BET} measurements.

UNISTRA conducted the electrochemical characterization of Mo_2C MXenes sourced from TCD. Two Mo_2C samples, produced via molten-salt etching using $CuCl_2$ and HCl, were analysed. These differed primarily in their etching times, 1.5 and 4 h, which likely resulted in varying oxidation levels and, consequently, different electrochemical performances. The electrochemical characterization was performed in an asymmetric system with activated carbon as the cathode material and Mo_2C MXenes as the anode material. 3 different electrolytes were evaluated: conventional sulfuric acid and 2 aqueous-based ionic liquids provided by SOLV: N111-TFO and pyr-TFO. The electrochemical performance was evaluated in terms of specific capacitance (in F/g), which was calculated from GCD curves at various current densities (**Figure 17**). Although the electrochemical performance of Mo_2C MXenes is favourable, with a specific capacitance~180 F/g at a current density~0.1 A/g, no significant differences were observed between the two samples with varying etching times or between the different electrolytes tested.

UNISTRA also conducted XPS analyses on Mo_2C MXenes obtained from TCD with two different etching times. The XPS analysis revealed that the surface oxygen content in both samples is similar,

corroborating the findings obtained by CNR. The similar oxygen content also accounts for the comparable electrochemical performance observed.

SOLV performed preliminary electrochemical investigations of a promising electrolyte 1M N_{1113}FSI in ACN with Skeleton's curved graphene electrodes (8.6 mg/cm² average active material mass loading) and compared this electrolyte to state-of-the-art electrolyte 1M $TEABF_4$ in ACN. At **SOLV**, GCD and CV measurements are performed on a Biologic BCS-805. EIS measurements were performed on a Biologic VMP3 from 10 mHz to 1 MHz with a sinus amplitude of 10mV. Firstly, CV was performed at 5 mV/s at different potentials (see **Figure 18**).

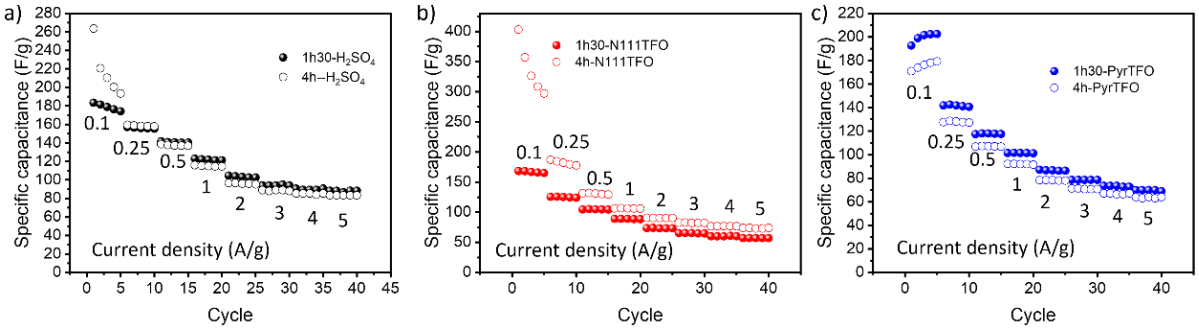

***Figure 17**. Specific capacitance of Mo_2C MXenes as a function of current density in a) sulfuric acid, b) N111-TFO (water) and c) pyr-TFO (water) electrolytes.*

Both electrolytes behave similarly and are stable up to 3.0V. The cell specific capacitance and energy density is the same for both electrolytes. EIS shows that both N_{1113}FSI and $TEABF_4$ demonstrate typical EDLC behaviours. However, N_{1113}FSI presents considerably higher electrolyte resistance represented by a larger semi-circle on the EIS. Above 3V, it appears as though 1M $TEABF_4$ in ACN is more stable than 1M N_{1113}FSI in ACN. Indeed, a decrease of current during the first moments of charge and discharge appears with N_{1113}FSI indicative of an increase in cell resistivity as indicated by the black arrows. Secondly, when N_{1113}FSI is cycled>3.5V, the current increases at the end of the charging process. This increase in current is indicative of faradaic reactions wherein current is irreversibly absorbed by the system, driving a chemical reaction. These faradaic reactions could be one or several different deleterious phenomena including the formation of a passivation layer on the electrode surface due to the oxidation of acetonitrile at high voltages, reduction of the effective surface, electrolyte decomposition (hydrolysis, polymerization, fluorination reactions, Hofmann elimination …), changes in the surface chemistry of the electrodes, electrochemical window limitations… Nonetheless from these preliminary tests, it appears as though N_{1113}FSI is compatible with CG and can be further explored and trialled with the project materials. One way of increasing the stability and performance of EDLC cells is by finetuning the electrode mass balancing as explored by BED.

SOLV performed similar floating tests on a batch BED's AC/FLG/CMC:SBR electrodes (85/10/5) using 1M N1113FSI in GVL with symetrical electrodes (m+/m- = 1) (see **Figure 19**). A marked decrease in energy efficiency was observed at 3.2V, consistent with BED's observations. In that system at 1A/g, a cell specific capacitance of 17.6 F/g and an energy density of 21.8 Wh/kg were measued at 2.8V. Typical EDLC behaviour was observed by cyclic voltamettry and by EIS. The increased viscosity of the GVL solvent compared to ACN reduces the capacitance and energy density of the cells considerably. Indeed, in the exact same conditions, changing solvents from ACN to GVL based electrolyte is accompanied by a decrease in capacitance and energy density of~14%.

Electrolyte formulations of $N_{1113}FSI$ in mixtures of GVL and ACN were produced with the perspective of combining the high flash point and green properties of GVL with the improved electrochemical performance and stability of ACN. For this, **SOLV** conducted flash point analysis (Eralytics Eraflash flash point tester). Indeed, electrolytes based solely on GVL present a flashpoint of 92°C whereas electrolytes based solely on ACN present dangerously low flash points of 10°C. For a point of comparison, pure ionic liquid show very high flashpoints (typically >250°C) (see D1.2). Flash point analysis of the results electrolytes show that even 5%$_m$ ACN content reduces the flash point of the electrolyte from 92°C to 58°C, **Figure 20**. A liquid is considered inflammable when the flash point is<60°C, making electrolytes with 95/5 GVL/CAN content inflammable. This flash point is further reduced when adding more ACN. No improvements were observed in terms of capacitance when adding small proportions of ACN to GVL electrolytes. For these reasons and purely from the electrolyte development point of view, other solvent bases will be explored.

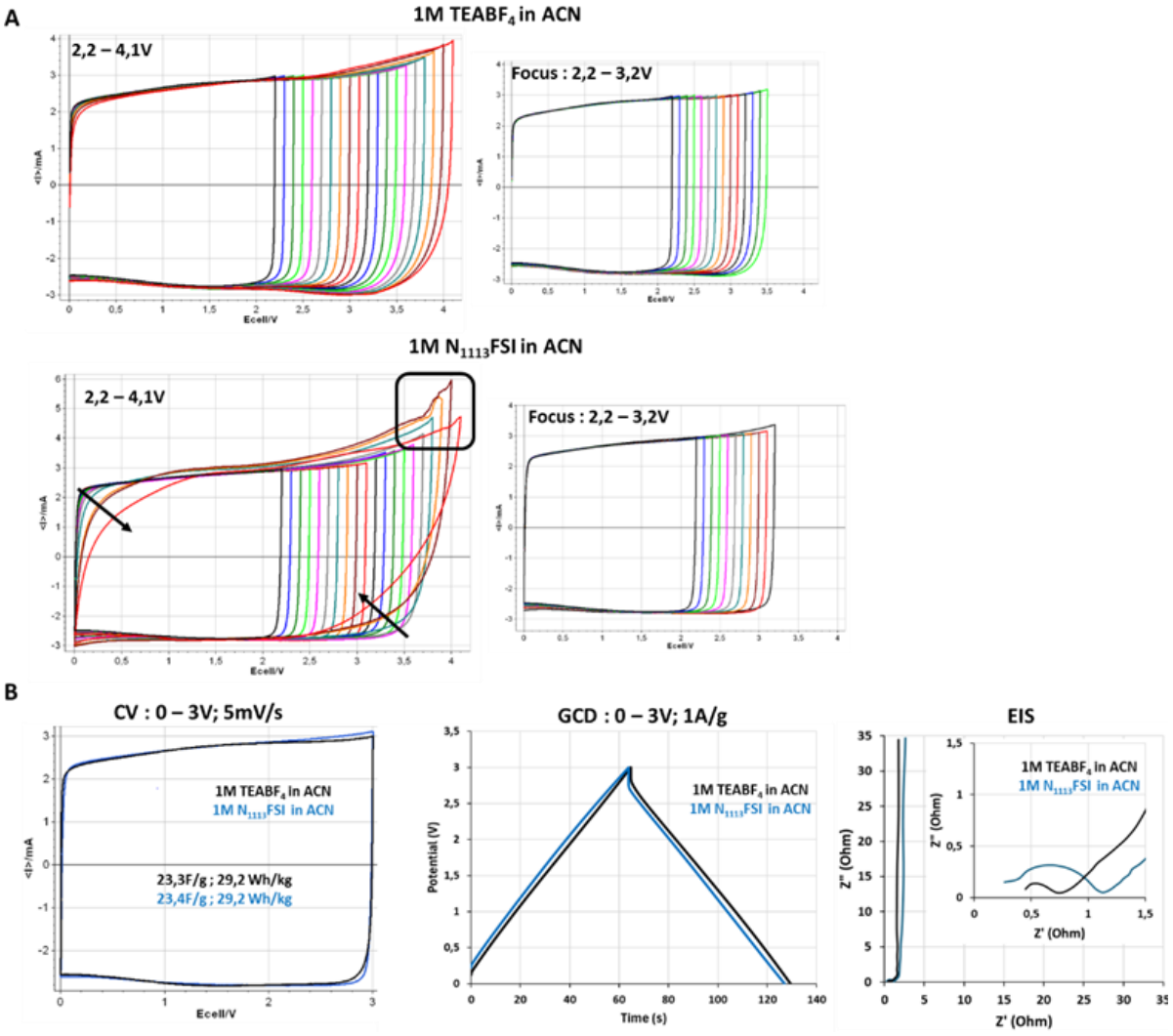

Figure 18. *(A) CV curves of 1M TEABF4 in ACN and 1M $N_{1113}FSI$ in ACN with Skeleton's CG electrodes (symmetrical electrode mass) at different potentials 5 mV/s at 25°C (10 CVs performed at each potential). (B) Comparison of CV (3V; 5mV/s), GCD (3V; 1A/g) and EIS of 1M TEABF4 in ACN and 1M $N_{1113}FSI$ in ACN with Skeleton's CG electrodes. Same electrode loading in each cell; AL-CVD CR2032 coin cell; 230µm GFA separator; 90µL electrolyte; 0.4mm spring; 1.0mm spacer.*

The ionic conductivities of the prepared electrolytes by **SOLV** were measured by **FSU** using a Binder KB53 climatic chamber and a BioLogic MPG-2 potentiostat from -30 to 80°C (**Figure 21**). As expected, conductivity increased with rising temperature. Among the electrolytes tested, 2 M N_{1113}FSI in ACN exhibited the highest conductivity across the temperature range, whereas the conductivity decreases as further increase in concentration. Besides, the conductivity values achieved with the selected concentrations (1 M and 2 M) of electrolytes are comparable to conventional electrolyte $TEABF_4$. Detailed electrochemical characterization after utilizing these electrolytes in cells is provided in WP2.

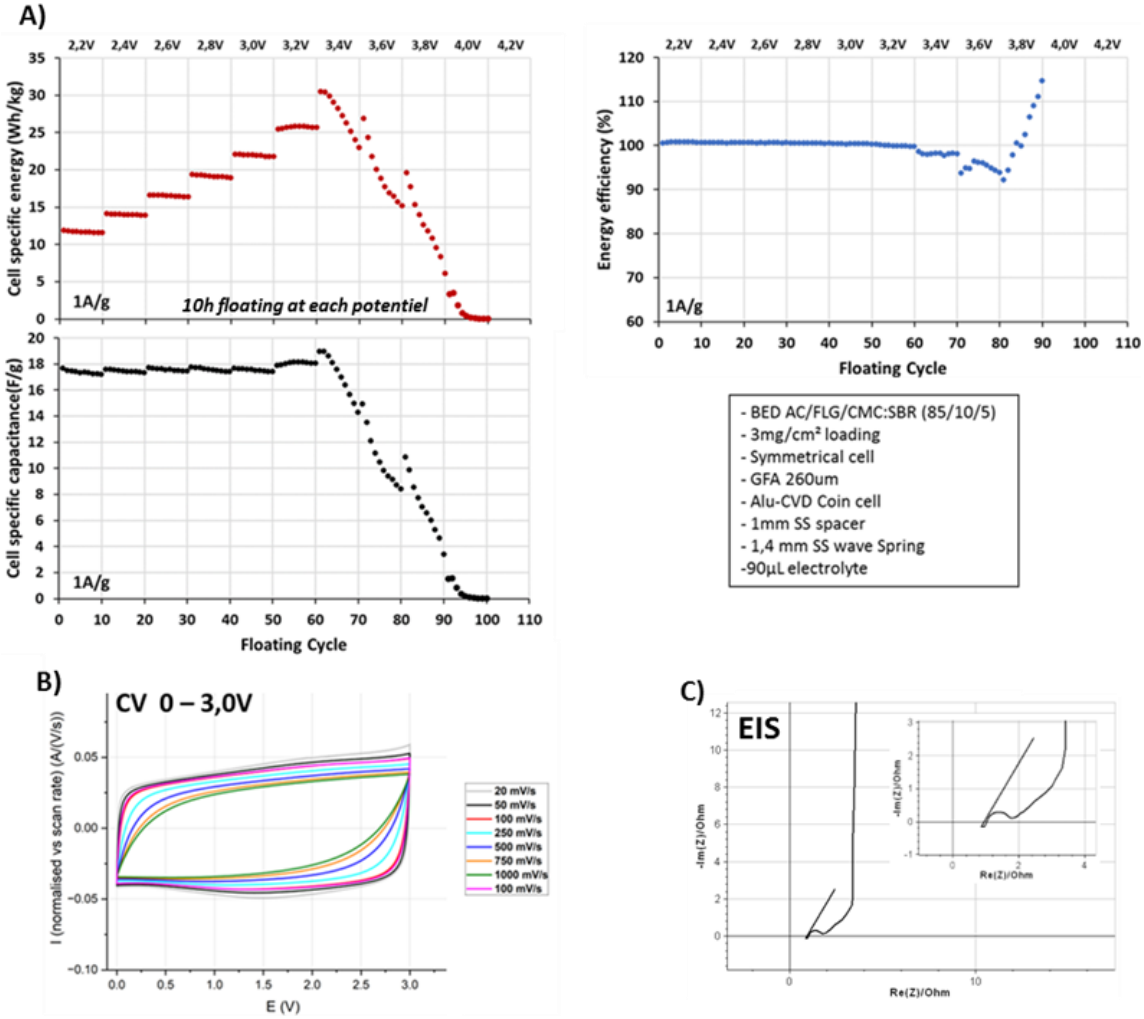

***Figure 19**. Overview of floating + galvanostatic stability tests (A), CV at different scan rates (B) and EIS (C) of a coin cell composed of BED's AC/FLG/CMC:SBR electrodes and 1M N_{1113}FSI in GVL.*

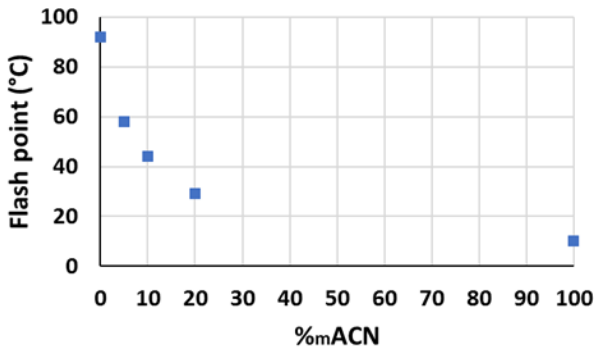

***Figure 20**. Flash point analysis of 1M N_{1113}FSI electrolytes in mixtures of ACN and GVL solvents.*

Ionic conductivity was also measured by **SOLV** as part of the development process for determining optimal electrolyte formulations. As to fine tune the electrolyte concentrations, the conductivities of a range of concentrations of N_{1113}FSI in acetonitrile were measured at different temperatures, **Figure 22**. The conductivity optimum was determined to be 2,0 mol/L N_{1113}FSI in ACN, consistent with FSU's observations. These tests confirm using a 2,0 mol/L N_{1113}FSI in ACN electrolyte for optimal conductivity. Ionic conductivity measurements were performed at **SOLV** on a Biologic SP300 with a Biologic ITS temperature control unit and a platinised HTCC probe. See D1.2 for more details.

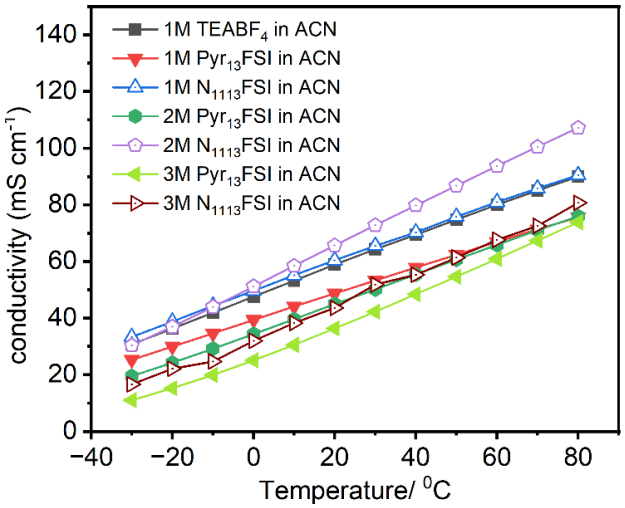

Figure 21. *Ionic conductivity within the temperature range of -30 °C to 80°C.*

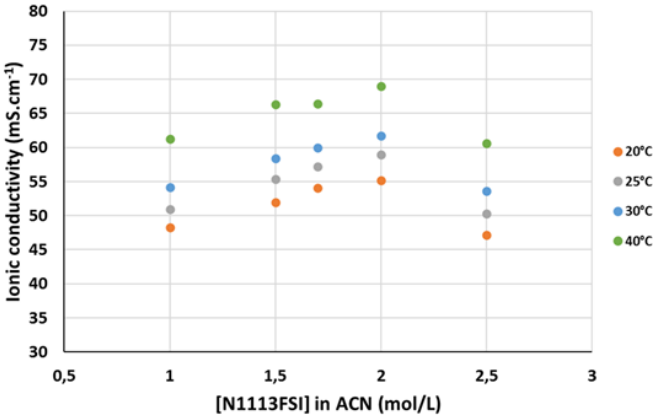

Figure 22*. Ionic conductivity of different concentrations of N1113FSI in ACN at different temperatures.*

Each IL produced by **SOLV** undergoes rigorous analysis to qualify and quantify any trace impurities including halides, sulfates, organic or acidic precursors, alkalines as well as water content. Electrolyte grade electrolytes are 99.9% pure and contain very low water content (typically <20ppm). For this, ionic chromatography and Karl Fisher analysis are systematically applied.

Different types of carbon-based materials from SM/SKL and BED and Mo_2C MXenes samples from TCD were characterised by **CNR**. Different SiC powders were structurally characterized at SpecXLab ISM CNR. Due to its unique crystal structure, SiC possesses advantages such as high temperature resistance, high mechanical strength, high thermal conductivity, high hardness, and chemical stability, which makes SiC-based SCs suitable for harsh environments and high temperatures. Currently, two SiC polytypes are accepted in SiC device research: 6H-SiC and 4H-SiC and with this constrain in mind SpecX-lab structurally characterized different SiC powders, namely SiC-04, Sic-05,

SiC-06, SiC-07 and SiC-08 (SKELETON). SiC-06, SiC-07 and SiC-08 powders present typical polycrystalline XRD patterns (as reported in **Figure 23**). Relative intensities of the different reflections within the same polycrystalline structure do not match the predicted theoretical values, thus suggesting the different powder structures are out of the thermodynamic equilibrium. Phases (4H-6H and 3C) are not equally represented in the analysed powders. In particular, SiC-06 exhibit dominant 3C phase; InSic-07 hexagonal phases are growing and become dominant SiC-08 (cubic phase negligible).

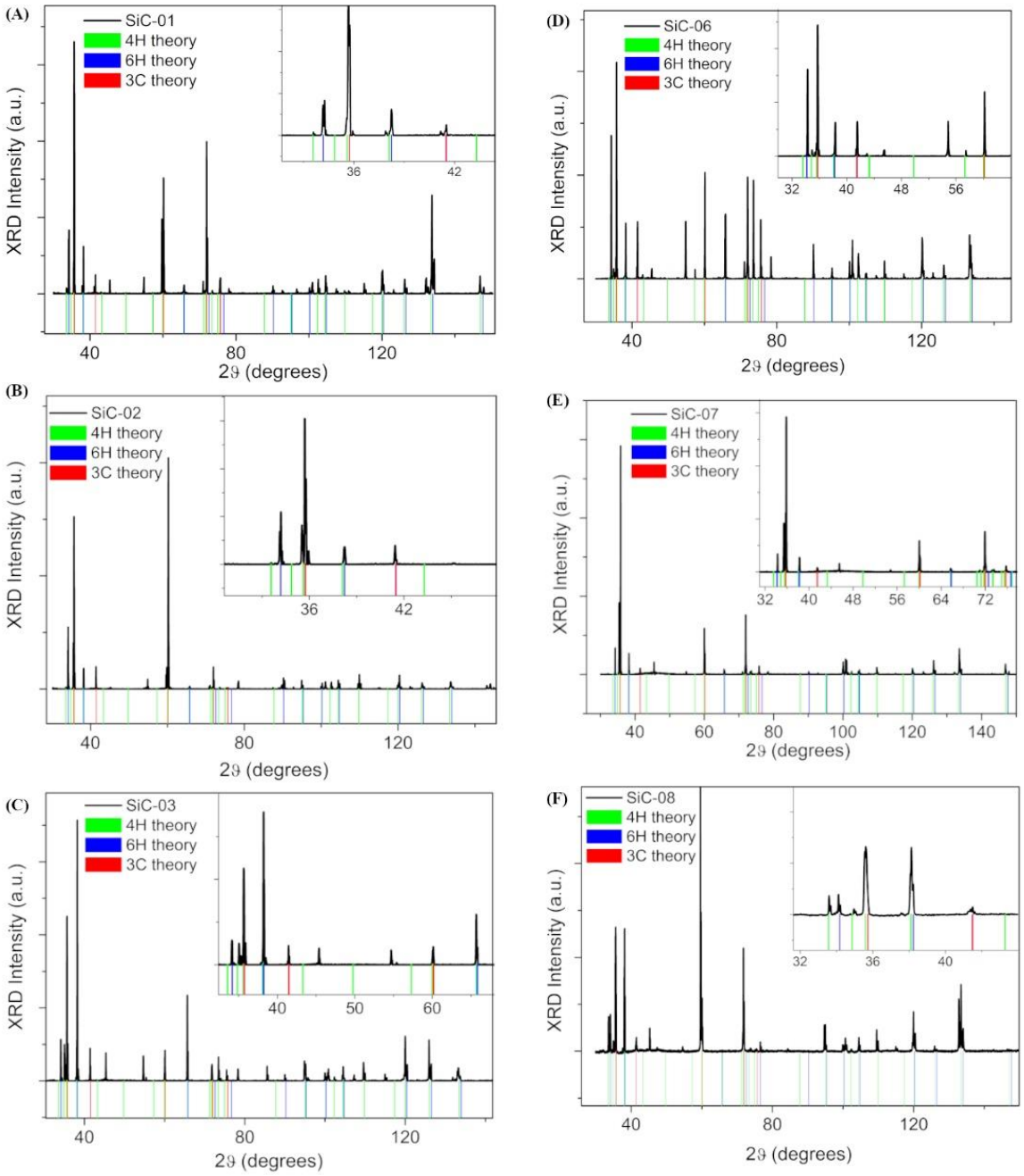

***Figure 23**. XRD patterns collected upon different SiC powders.*

When SiC-01, 02 and 03 are considered, cubic crystallites are always bigger than the hexagonal. For Sic-06, 07 and 08 the hexagonal crystallites are always of comparable dimensions independently on being 4H or 6H and cubic crystallites are always smaller than the hexagonal. Furthermore, overall

crystallite size grows passing from Sic-01 to SiC-03 and from SiC 06 to SiC 08 (despite the smaller visible morphology of the powder for the latter sample).

Single particle advanced XRD and rocking curve analysis (Omega-2Theta scan) were performed by means of a Eulerian cradle upon SiC powders nr 04 and 05 showing large particles. SiC 04 dispersion is composed of several large particles each one composed differently oriented crystallites. Specifically, the largest particle was studied by mean of in plane rotations and RC analysis and turned out to be individually composed of 6H monocrystalline hexagonal crystallites. Results are reported in **Figure24**.

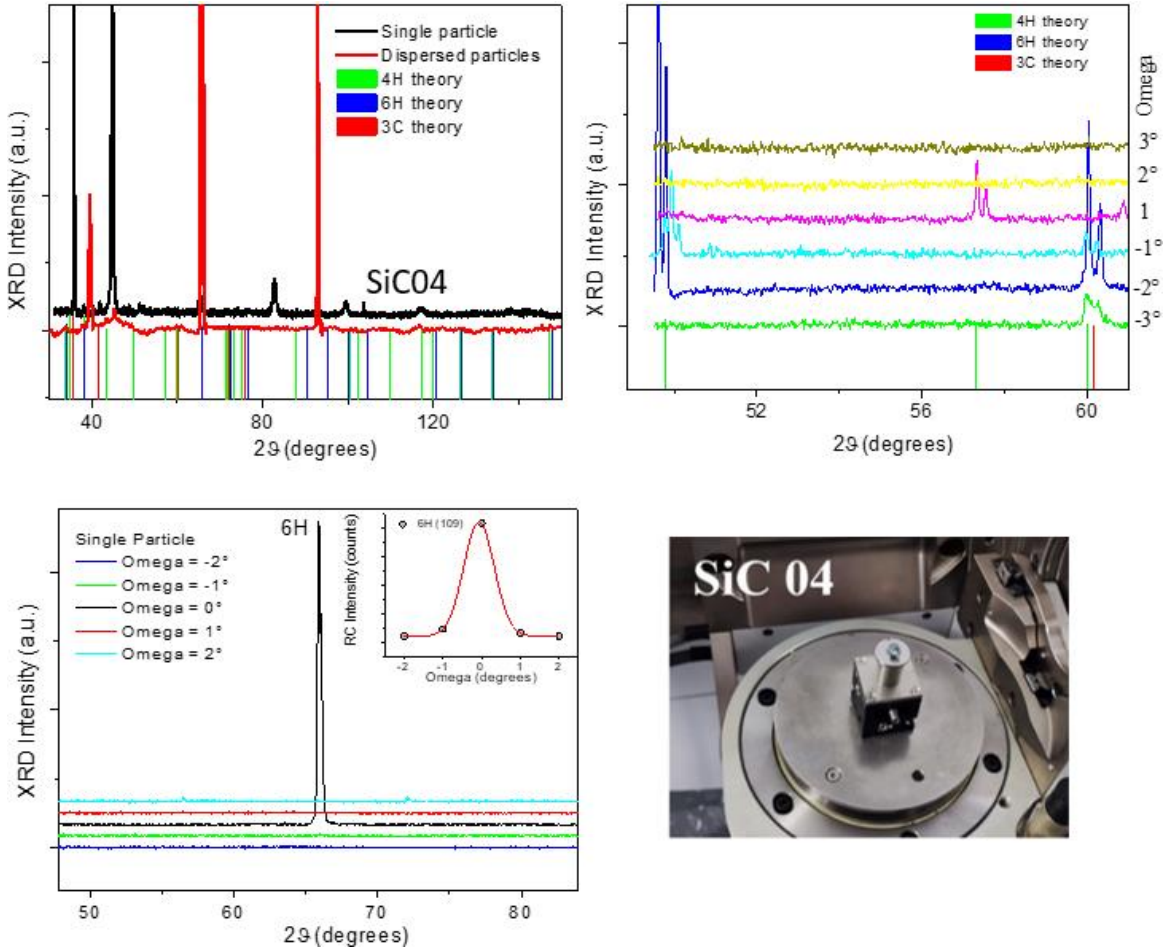

***Figure 24**. XRD patterns collected upon $SiC0_4$ powder/single particle. RC analysis of powder and single particle is also reported.*

The same experimental procedure for sample SiC 05 indicated that SiC05 particles are characterized by SiC hexagonal 6H phase only, and each particle is composed of differently oriented crystallites as reported in **Figure 25.** Grains size calculation was performed for all analyzed samples and turns smaller passing from SiC-04 to 08 as reported in **Table 1**.

***Table 1**. Average grain size deduced for each sample.*

Sample	4H (101)	6H (101)	3C (111)
SiC-01	120nm	180nm	220nm
SiC-02	180nm	240nm	230nm
SiC-03	210nm	250nm	310nm
SiC-06	185nm	185nm	110nm
SiC-07	200nm	215nm	150nm
SiC-08	250nm	260nm	200nm

In conclusion, SiC-01, 02, and 03 powders are polycrystalline with cubic crystallites always bigger than the hexagonal Sic-06, 07 and 08 powders are polycrystalline with the cubic crystallites always smaller than the hexagonal. SiC 04 dispersion comprises several large particles each composed of differently oriented crystallites.

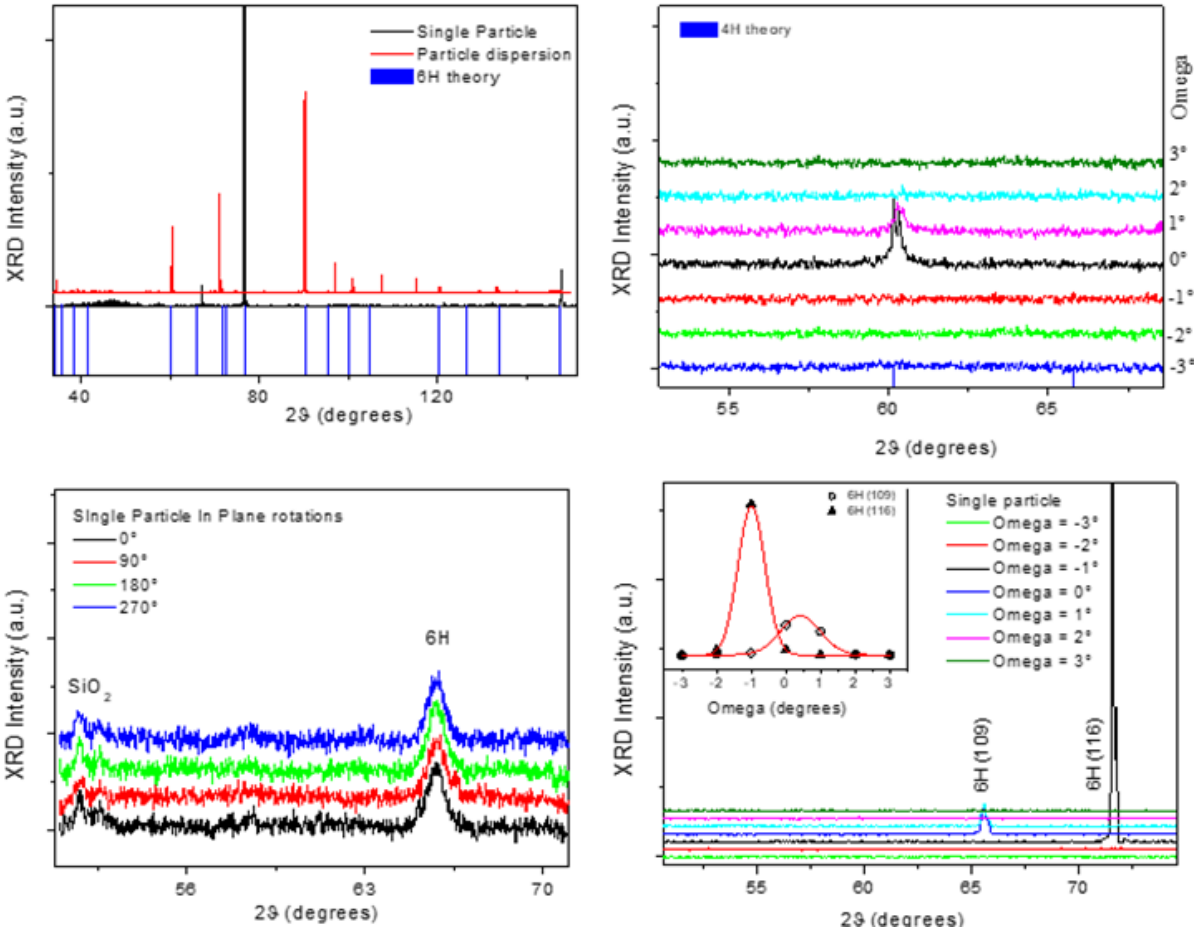

***Figure 25**. XRD patterns collected upon SiC05 powder/single particle. RC analysis of powder and single particle is also reported as well as the in-plane symmetry study.*

One of the largest particles, chosen for RC analysis, turned out to be individually composed of 6H monocrystalline hexagonal crystallites of small size if compared to other samples. The SiC05 dispersion is characterized by SiC hexagonal 6H phase only. This is confirmed by RC analysis of the largest particle showing monocrystalline structure with hexagonal 6H phase only.

A photoemission spectroscopy analysis with synchrotron radiation was required to evaluate the residual content of Cl in differently treated types of CG. To determine quantitatively the presence of Cl, thick layers of the powder samples were deposited on carbon tape and analysed by photoemission spectroscopy using hv = 510 eV. This energy was carefully chosen to avoid the overlap of the weak Cl 2p levels with other spectroscopic features, such as Auger transition peaks.

Figure 26 displays survey, C 1s and Cl 2p spectra for the unmilled (pristine, ID 5359), milled N_2 (ID 5458), milled air (ID 5459), H_2 treated N_2 (ID 5460) and H_2 treated air (ID 5461) powders. All samples consist basically of carbon, which is the only element giving rise to a well-defined peak in the survey spectra. The C 1s spectra have a lineshape compatible with the presence of a predominant C=C component at lower binding energies (~284.5 eV) and a smaller and broader C –C component at higher binding energies (~285eV). For the present analysis, it is not necessary to proceed with fitting the C 1s

peaks, as the Cl 2p content will be determined with respect to the overall C content. Thanks to the high brilliance of the synchrotron light, it is possible to show the presence of weak Cl 2p levels. The H_2 treatments are very efficient in reducing the Cl content.

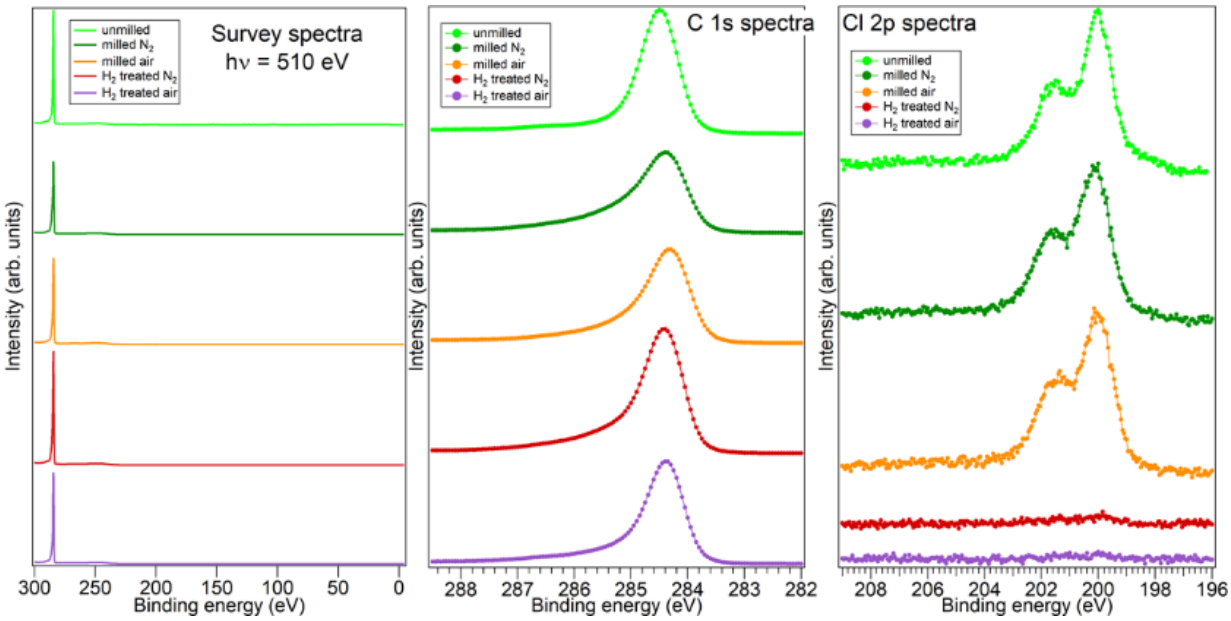

Figure 26. *C 1s and Cl 2p spectra acquired with hν = 510 eV for differently treated types of CG.*

Table 2 reports the total areas of the C 1s and Cl 2p peaks, their ratios and their ratios normalized to the respective photoemission cross sections (σC1s (510 eV) = 0.26 and σCl2p (510 eV) = 0.66 give a normalization factor of 0.39). The C 1s and Cl 2p peaks areas are taken in the energy ranges 283- 288 eV and 192.2÷206.8 eV, respectively. The last two rows are the quantities requested by SM/SKL.

Table 2. *Total areas of the C 1s and Cl 2p peaks and their ratios for the differently treated CG samples.*

Sample	unmilled	milled N_2	milled air	H_2 treated N_2	H_2 treated air
C1s total area (× 10^6)	1.06	0.94	0.98	1.24	0.95
Cl2p total area (× 10^3)	1.09	1.10	1.10	0.05	0.03
Cl2p/C1s (× 10^{-3})	1.03	1.17	1.12	0.04	0.03
0.39×Cl2p/C1s (× 10^{-4})	4.02	4.56	4.37	0.16	0.12
Cl/C (%)	0.0402	0.0456	0.0437	0.0016	0.0012

Through peak fitting it is possible to determine the chemical state of the observed Cl content, **Fig. 27.** Before H_2 treatment (unmilled, milled N_2, and milled air samples) we can describe the spectra with three doublets located at about (position of the Cl $2p_{3/2}$ component): 198.50, 200.00, and 201.05 eV. The main doublet can be attributed to Cl covalently bonded to C. The doublet at lower binding energy can be associated with physisorbed Cl. The last doublet could be due to Cl-C=O. The ratio between these three doublets changes slightly as a function of the treatments. Big changes are observed after H_2 treatment, which induces a strong suppression of the Cl 2p signal. In this case, the low statistics

allow us to identify safely only one doublet, corresponding to the main doublet observed in the previous spectra (slightly shifted to lower binding energies).

Table 3 summarize the results of the Cl 2p peak fitting.

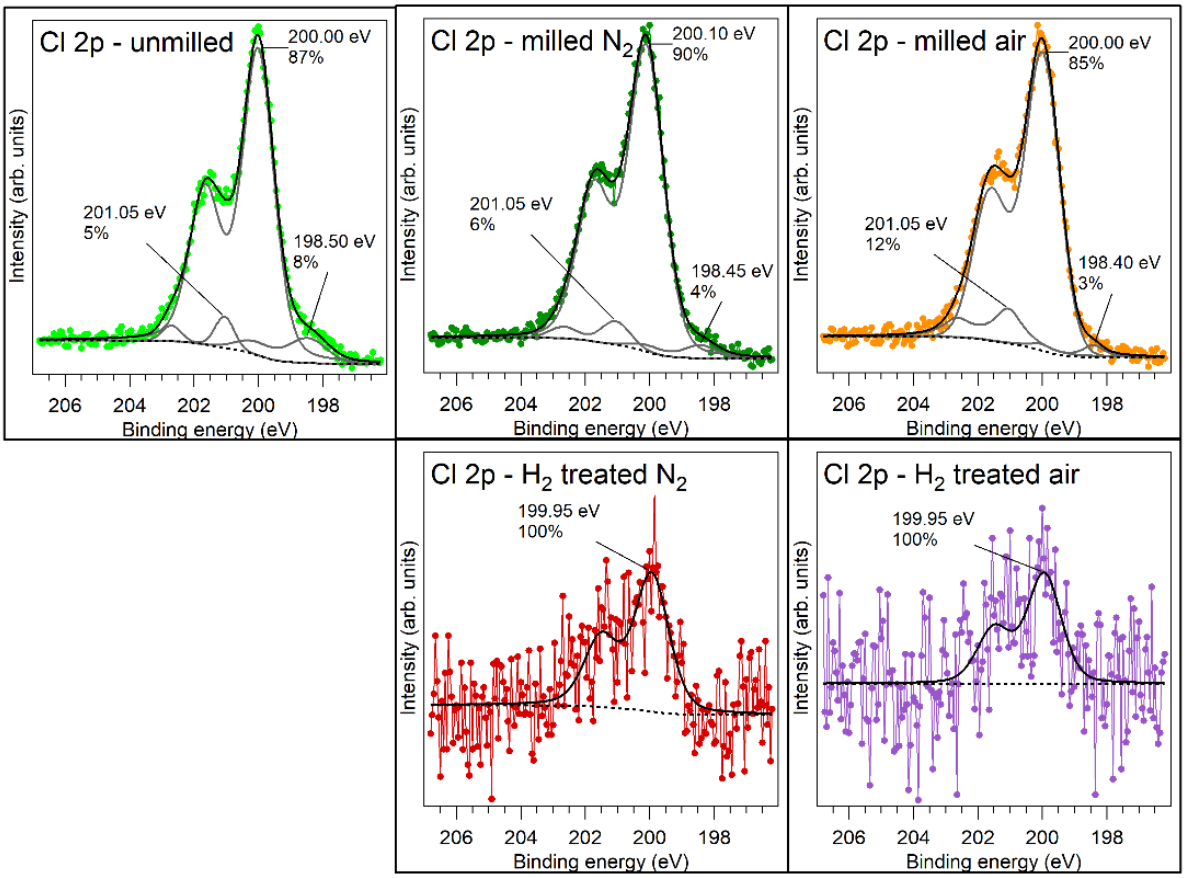

***Figure 27**. Peak fitting procedure for the Cl 2p spectra reported*

***Table 3**. Relative presence of Cl species for the differently treated CG samples.*

Sample	Unmilled	Milled N_2	Milled air	H_2 treated N_2	H_2 treated air
physisorbed Cl	8%	4%	3%	0%	0%
Cov. bonded Cl	87%	90%	85%	100%	100%
Cl-C=O	5%	6%	12%	0%	0%

ISM-CNR started another activity in collaboration with BED and SM/SKL concerning the exploration of the electronic structure of different carbon-based materials. The study intends to correlate the fundamental properties and capacitive behaviour of the materials, labelled as follows:

Sample A: FLG (from BED)

Sample B: FLG thermally treated with H_2 in Ar (from BED)

Sample C: AC (from BED)

Sample D: AC thermally treated with H_2 in Ar (from BED)

Sample H: CG unmilled (from SM)

Sample I: CG milled in N_2 (from SM)

Sample J: CG milled in air (from SM)

Sample K: CG thermally treated with H_2 in N_2 (from SM)

Sample L: CG with H_2 in air (from SM)

All samples were deposited on carbon tape and analyzed by photoemission spectroscopy with synchrotron radiation at hv = 450 eV (C 1s) and hv = 50 eV (valence band). **Figure8** and **Figure29** summarize the data collected on the materials received from BeD and SKELETON, respectively.

From the analysis of the C 1s spectra we observe that the sp2 component, which has the lowest binding energy among the C-related components, changes as a function of the treatments. The most significant change is observed if we compare activated carbon (samples C and D in **Figure28**) with curved graphene (samples I-L in **Figure29**). In curved graphene the binding energy of the sp2 component is significantly lower with respect to activated carbon. In sample J the sp2 component is at 284.25 eV, while in sample D it is at 284.55 eV. This difference has a counterpart in the valence band. The valence band spectra of the samples present a peak in the range of 2-4 eV and a well-defined Fermi level (visible in the logarithmic plot of the data, not shown). The peak represents the bottom of the π states, which are responsible for the transport properties of the material. For curved graphene the peak maximum is located at about 2.85 eV (sample J), while in activated carbon (samples C and D) it is located at about 3.2 eV. As the density of states of the π states decreases while approaching the Dirac point, the position of the band bottom at lower binding energy could be connected to a higher density of states in curved graphene than in activated carbon. These results must be considered preliminary. Further data collection and analysis is planned in the next period.

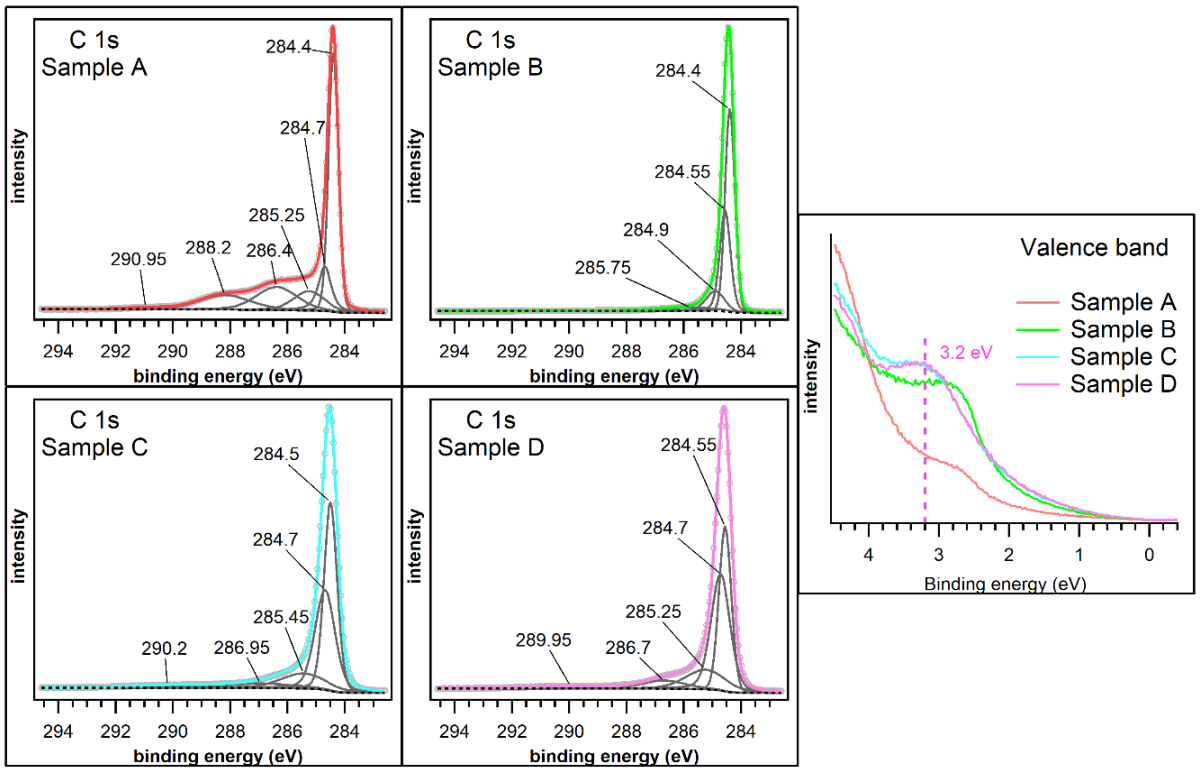

***Figure28**. C 1s and valence band spectra acquired on samples A, B, C and D at 450 and 50eV.*

Structural characterization of differently treated MoC_2 samples (TCD) was performed at SpecXLab ISM CNR. Specifically, molybdenum carbide powders/pellets were investigated, and their structures were compared as a function of the following treatments: 1) $CuCl_2$ + HCl 4h; 2) $CuCl_2$ + HCl 1.5h; 3) APS 1.5h. XRD patterns collected on pellet (left panel) and powder (right panel) samples are reported in **Figure 30.** Mo_2C crystalline signatures are detected (JCDD card number 00-011-0680 -crystal system: hexagonal). Signatures of cubic MoO_2 (labelled by red asterisks) were also observed when $CuCl_2$ + HCl 4h and APS 1.5h treatments are used. Conversely, no evidence of the presence of oxides compounds

was found in the samples treated with $CuCl_2$ + 1.5h HCl, preserving the MoC_2 theoretical structure only. Comparison between pellet and powder XRD patterns revealed no evident changes but a decrease in the (200)/(101) intensity ratios for all the powder samples, regardless of the type of treatment.

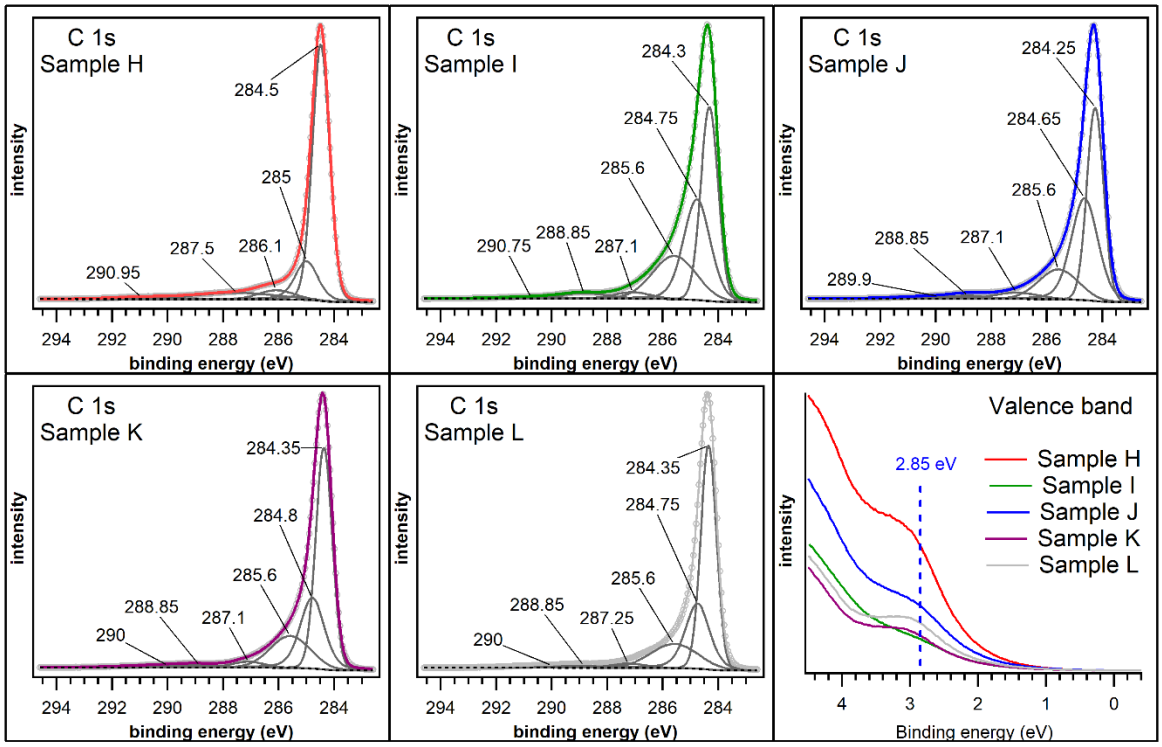

Figure29. C 1s and valence band spectra acquired on samples G, H, I, J and K at 450 and 50 eV.

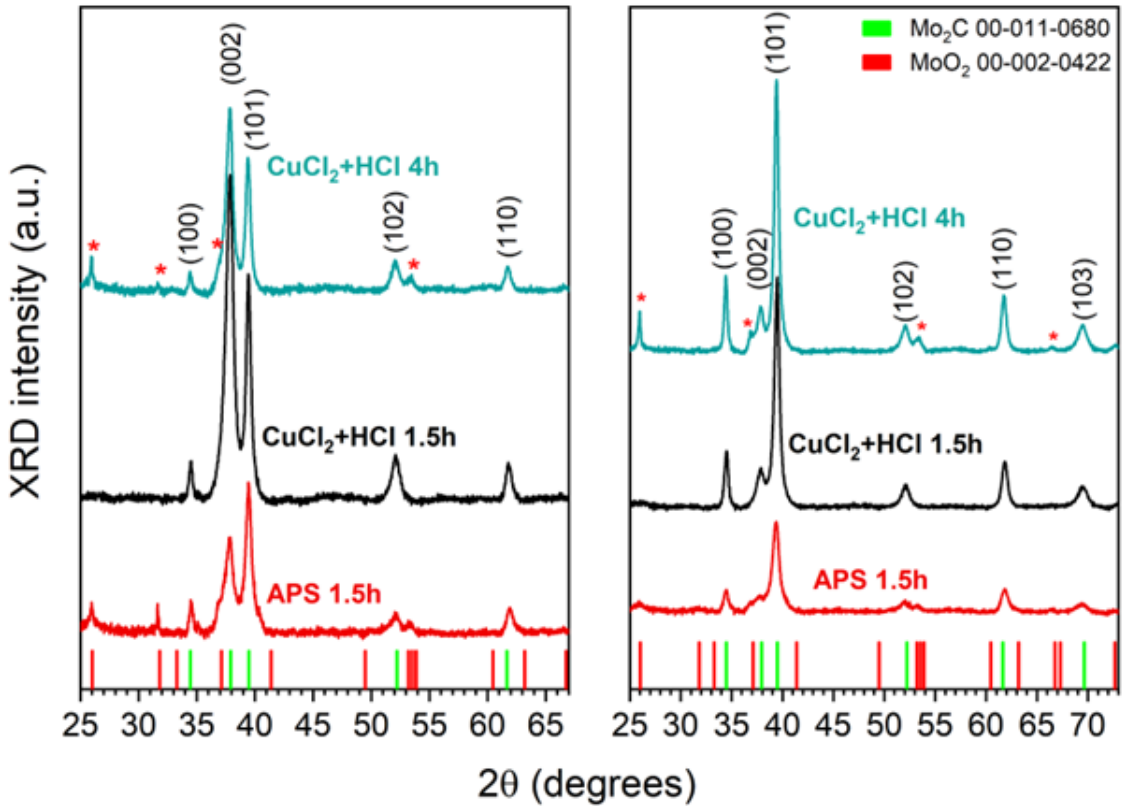

Figure 30. XRD pattern collected on Mo_2C (left) pellet and (right) powder samples: $CuCl_2$+HCl 4h (blue line), $CuCl_2$+HCl 1.5h (black line) and APS 1.5h (red line).

Table 4. Comparison between the (200)/(101) intensity ratios measured for pellet and powder

Sample	I(002)/I(101) PELLET	I(002)/I(101) POWDER
$CuCl_2$ + HCl 4h	1.3	0.16
$CuCl_2$ + HCl 1.5h	1.5	0.15
APS 1.5h	0.6	0.17

The same type of Mo_2C samples from TCD were analyzed at the VUV-Photoemission beamline of the Elettra synchrotron radiation facility. In this case, the samples consisted of thick layers of Mo_2C powders deposited on Cu plates. All data were collected at 750 eV. Survey spectra (**Figure 31**) show the presence of the expected elements (O, C, Mo, Cl) for all samples. Notably, from the spectroscopic point of view, the samples look very similar. For all samples, we could fit the different core level lines with the same number of peaks or doublets, except the Cl 2p line.

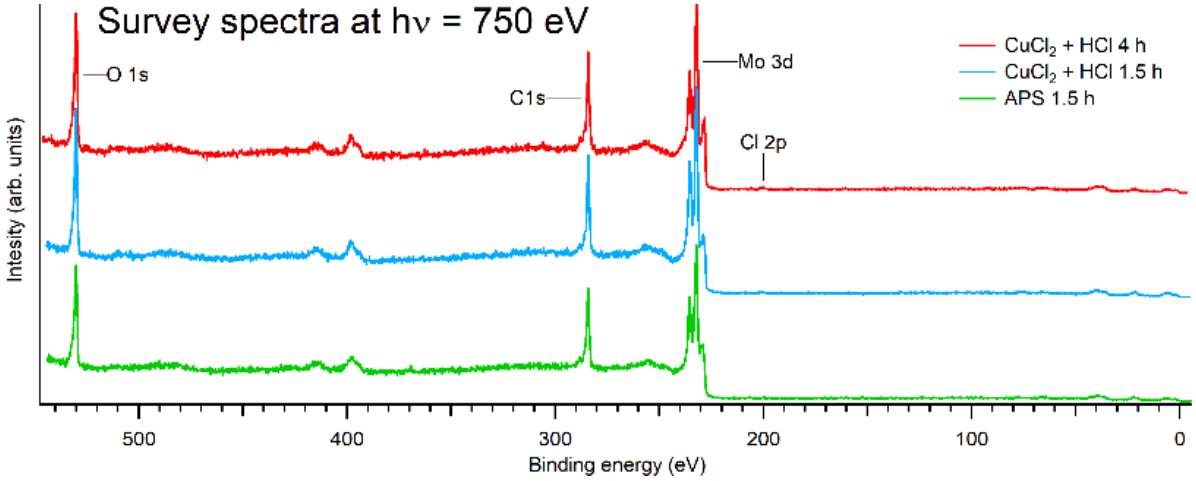

Figure 31. Survey spectra of the $CuCl_2$ + HCl 4h, $CuCl_2$ + HCl 1.5h and APS 1.5h samples at hv = 750 eV.

Figure 32 plots the relevant core level lines and related fittings for the $CuCl_2$ + HCl 4h sample. The O 1s spectrum can be fitted with 3 peaks. The red peak (530.1 eV) corresponds to Mo-oxides, the blue peak (530. 875 eV) to C-Mo-O and C-Mo-(OH) bonds and the green one (532.55 eV) to adsorbed water. The C 1s spectrum can be fitted with 4 peaks. The orange peak (283 eV) corresponds to C in Mo_2C, the red peak (284.1 eV) to C-C bonds, the blue peak (285.075 eV) to C-H bonds and the green one (287.9 eV) to CO and COOH. The Mo 3d spectrum can be described with 4 main doublets. The blue doublet (Mo $3d_{5/2}$ at 228.075 eV) corresponds to metallic Mo, the orange (Mo $3d_{5/2}$ at 228.825 eV) to Mo in Mo_2C, the green doublet (Mo $3d_{5/2}$ at 230 eV) to Mo in MoO_2 and the red doublet (Mo $3d_{5/2}$ at 232.175 eV) to Mo in MoO_3. The Cl 2p spectrum presents 2 doublets: the red doublet (Cl $2p_{3/2}$ at 200.05 eV) is associated to covalently bonded Cl and the blue doublet (Cl $2p_{3/2}$ at 198.5 eV) to physisorbed Cl.

Figure 33 reports the relevant core level lines and related fitting for the $CuCl_2$ + HCl 1.5h sample. The O 1s spectrum can be fitted with 3 peaks. The red peak (530.225 eV) corresponds to Mo-oxides, the blue (531.125 eV) to C-Mo-O and C-Mo-(OH) bonds and the green (532.375 eV) to adsorbed water. The C 1s spectrum can be fitted with 4 peaks. The orange peak (283.1 eV) corresponds to C in Mo_2C, the red (284.15 eV) to C-C bonds, the blue (285.25 eV) to C-H bonds and the green (288.1 eV) to CO and COOH. The Mo 3d spectrum can be described with 4 main doublets. The blue doublet (Mo $3d_{5/2}$ at 228.125 eV) corresponds to metallic Mo, the orange (Mo $3d_{5/2}$ at 228.875 eV) to Mo in Mo_2C, the green (Mo $3d_{5/2}$ at 230 eV) to Mo in MoO_2 and the red (Mo $3d_{5/2}$ at 232.25 eV) to Mo in MoO_3. The

Cl 2p spectrum presents 2 doublets: the red doublet (Cl $2p_{3/2}$ at 200 eV) is associated to covalently bonded Cl and the blue one (Cl $2p_{3/2}$ at 198.25 eV) to physisorbed Cl.

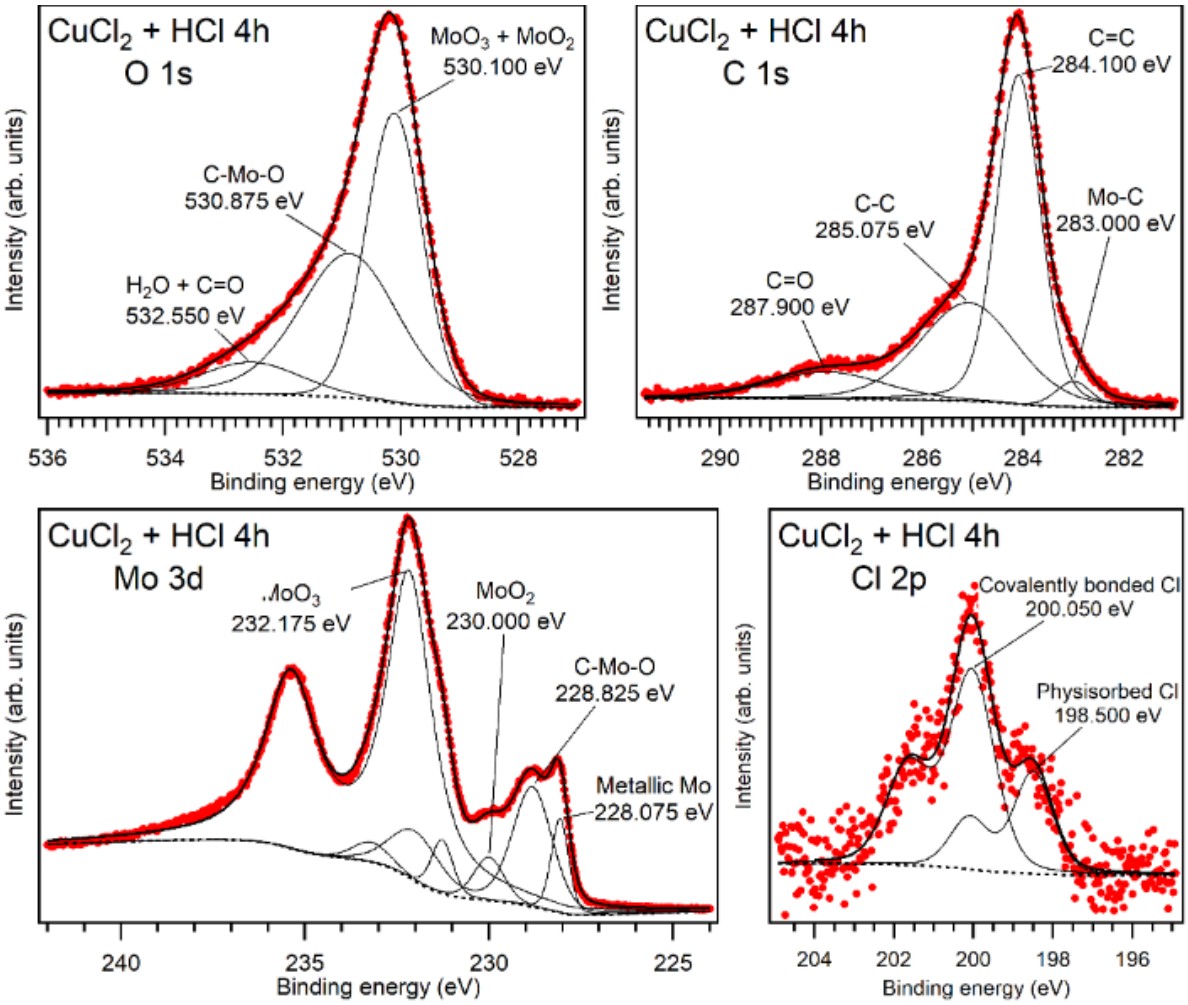

***Figure 32**. O 1s, C 1s, Mo 3d and Cl 2p high-resolution core level lines and related fittings for the $CuCl_2$ + HCl 4h sample.*

Figure 34 reports the relevant core level lines and related fitting for the APS 1.5h sample. The O 1s spectrum can be fitted with 3 peaks. The red peak (530.225 eV) corresponds to Mo-oxides, the blue (530.95 eV) to C-Mo-O and C-Mo-(OH) bonds and the green (532.45 eV) to adsorbed water. The C 1s spectrum can be fitted with 4 peaks. The orange peak (283.325 eV) corresponds to C in Mo_2C, the red (284.25 eV) to C-C bonds, the blue (285.175 eV) to C-H bonds and the green (288.075 eV) to CO and COOH. The Mo 3d spectrum can be described with 4 main doublets. The blue doublet (Mo $3d_{5/2}$ at 228.15 eV) corresponds to metallic Mo, the orange (Mo $3d_{5/2}$ at 228.975 eV) to Mo in Mo_2C, the green (Mo $3d_{5/2}$ at 230.05 eV) to Mo in MoO_2 and the red (Mo $3d_{5/2}$ at 232.325 eV) to Mo in MoO_3. The Cl 2p spectrum presents only one red doublet (Cl $2p_{3/2}$ at 200.125 eV) is associated to covalently bonded Cl.

The analysis reveals that the 3 different preparations have a moderate impact on the composition of the samples. The Mo 3d spectrum is dominated by Mo-oxide peaks (especially MoO_3). The Mo_2C content is small, if compared to the Mo-oxides. There is an additional component of metallic Mo. From the ratio of the doublets, we can say that the APS 1.5h sample has the highest Mo_2C and the lowest metallic Mo content. This sample has also the lowest Cl content.

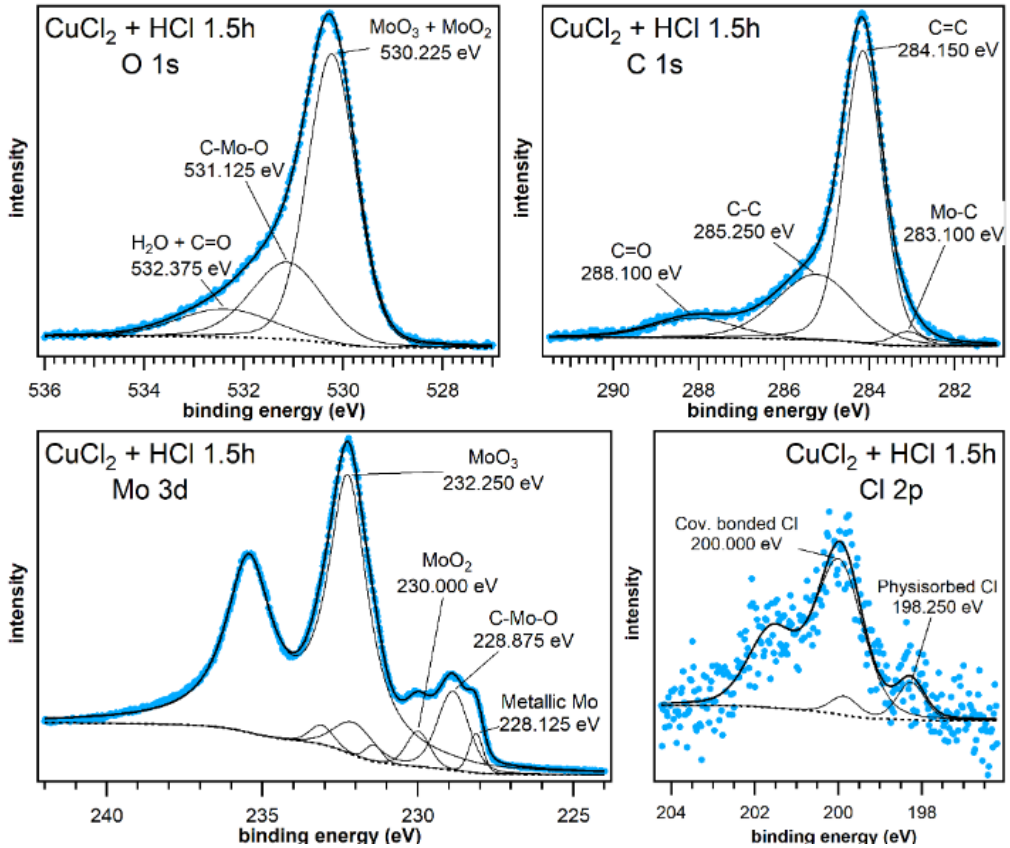

***Figure 33**. O 1s, C 1s, Mo 3d and Cl 2p high-resolution core level lines and related fittings for the $CuCl_2$ + HCl 1.5h sample.*

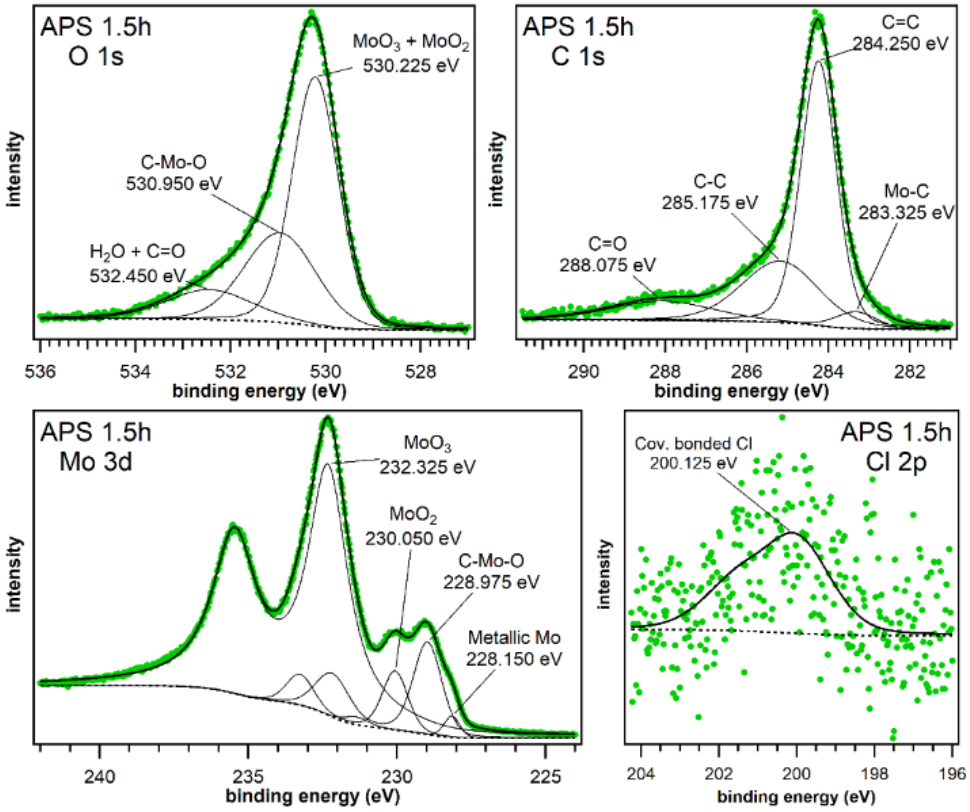

***Figure 34**. O 1s, C 1s, Mo 3d and Cl 2p high-resolution core level lines and related fittings for the APS 1.5h sample*

3 Results & Discussion

3.1 Results

D1.3 contributes to achieving several objectives outlined in the GREENCAP DoA. By providing comprehensive multiscale physicochemical and electrochemical characterizations of EMs and electrolytes, it aligns with the goal of developing sustainable, high-performance SCs with enhanced energy density, power density, and cycle life. The detailed insights into the composition, structure, morphology, and electrochemical behaviour of these materials underpin the optimization of layered materials and ionic liquid -based interfaces, central to achieving the project's technological milestones. Furthermore, D1.3 supports the objective of validating material properties under industrially relevant conditions, laying the groundwork for scalability, reliability, and integration into circular economy frameworks.

3.2 Contribution to project (linked) Objectives

The multiscale characterization methods and results establish a standardized framework for assessing advanced materials, offering reproducible and transferable protocols. These are critical for scaling up material production and ensuring consistent performance in supercapacitor applications.

The detailed understanding of material properties facilitates the rational design of hybrid electrodes, combining graphene, MXenes, and functionalized components. This contributes to the development of SCs with improved energy and power densities, which can meet and exceed current industry benchmark

3.3 Contribution to major project exploitable result

The methodologies and findings from this deliverable expand the scientific knowledge base, offering insights into charge storage mechanisms at layered materials and ionic liquid interfaces. This aids in advancing the field of energy storage and informs future research directions.

4 Conclusion and Recommendation

D1.3 provided a comprehensive multiscale characterization of electrode materials and electrolytes, it has delivered critical insights into their composition, structure, morphology, and electrochemical properties. These findings form the basis for optimizing layered materials and ionic liquid -based interfaces, directly supporting the project's objectives. The standardized characterization methodologies established in this deliverable ensure reproducibility and scalability, enabling the transition from laboratory innovations to industrial-scale applications. The data and methodologies also underpin the rational design of hybrid electrodes contributing to the development of SCs that exceed current industry benchmarks.

5 Acknowledgement

The author(s) would like to thank the partners in the project for their valuable comments on previous drafts and for performing the review.

Project partners:

#	Partner short name	Partner Full Name
1	BED	BEDIMENSIONAL SPA
2	SOLV	SOLVIONIC
3	FSU	FRIEDRICH-SCHILLER-UNIVERSITAT JENA
4	SKL	SKELETON TECHNOLOGIES OU
5	TCD	THE PROVOST, FELLOWS, FOUNDATION SCHOLARS & THE OTHER MEMBERS OF BOARD, OF THE COLLEGE OF THE HOLY & UNDIVIDED TRINITY OF QUEEN ELIZABETH NEAR DUBLIN
6	TUD	TECHNISCHE UNIVERSITAET DRESDEN
7	UNISTRA	UNIVERSITE DE STRASBOURG
8	SM	SKELETON MATERIALS GMBH
9	UNR	UNIRESEARCH BV
10	CNR	CONSIGLIO NAZIONALE DELLE RICERCHE
11	UCAM	THE CHANCELLOR MASTERS AND SCHOLARS OF THE UNIVERSITY OF CAMBRIDGE
12	CU	Y CARBON LLC

This project has received funding from the European Union's Horizon Europe research and innovation programme under grant agreement No 101091572. Views and opinions expressed are however those of the author(s) only and do not necessarily reflect those of the European Union. Neither the European Union nor the granting authority can be held responsible for them.

6 Appendix A - Quality Assurance Review Form

The following questions should be answered by all reviewers (WP Leader, reviewer, Project Coordinator) as part of the Quality Assurance procedure. Questions answered with NO should be motivated. The deliverable author will update the draft based on the comments. When all reviewers have answered all questions with YES, only then can the Deliverable be submitted to the EC.

NOTE: This Quality Assurance form will be removed from Deliverables with dissemination level "Public" before publication.

Question	WP Leader	Reviewer	Project Coordinator
	Prof. Valeria Nicolosi (TCD)	Ali Shaygan Nia (TUD)	Francesco Bonaccorso (BeD)
1. *Do you accept this Deliverable as it is?*	Yes	Yes	Yes
2. *Is the Deliverable complete?* - *All required chapters?* - *Use of relevant templates?*	Yes	Yes	Yes
3. *Does the Deliverable correspond to the DoA?* - *All relevant actions preformed and reported?*	Yes	Yes	Yes
4. *Is the Deliverable in line with the GREENCAP objectives?* - *WP objectives* - *Task Objectives*	Yes	Yes	Yes
5. *Is the technical quality sufficient?* - *Inputs and assumptions correct/clear?* - *Data, calculations, and motivations correct/clear?* - *Outputs and conclusions correct/clear?*	Yes	Yes	Yes
6. *Is created and potential IP identified and are protection measures in place?*	Yes	Yes	Yes
7. *Is the Risk Procedure followed and reported?*	Yes	Yes	Yes
8. *Is the reporting quality sufficient?* - *Clear language* - *Clear argumentation* - *Consistency* - *Structure*	Yes	Yes	Yes